AGU PUBLICATIONS

JGR

Journal of Geophysical Research: Solid Earth

RESEARCH ARTICLE
10.1002/2015JB012258

Key Points:
- CO_2 fluxes at the surface are highly sensitive to the dissolved CO_2 content of the deep fluid
- The sensitivity of CO_2 fluxes on reservoir geometry depends on the depth of gas exsolution
- Heat conduction and isenthalpic volume expansion balance the heat carried by CO_2

Correspondence to:
L. Peiffer,
loic.peiffer@gmail.com

Citation:
Peiffer, L., C. Wanner, and L. Pan (2015), Numerical modeling of cold magmatic CO_2 flux measurements for the exploration of hidden geothermal systems, *J. Geophys. Res. Solid Earth*, *120*, 6856–6877, doi:10.1002/2015JB012258.

Received 3 JUN 2015
Accepted 9 SEP 2015
Accepted article online 11 SEP 2015
Published online 20 OCT 2015

Numerical modeling of cold magmatic CO_2 flux measurements for the exploration of hidden geothermal systems

Loïc Peiffer[1], Christoph Wanner[2], and Lehua Pan[3]

[1]Instituto de Energías Renovables, Universidad Nacional Autónoma de México, Temixco, Mexico, [2]Institute of Geological Sciences, University of Bern, Bern, Switzerland, [3]Lawrence Berkeley National Laboratory, Berkeley, California, USA

Abstract The most accepted conceptual model to explain surface degassing of cold magmatic CO_2 in volcanic-geothermal systems involves the presence of a gas reservoir. In this study, numerical simulations using the TOUGH2-ECO2N V2.0 package are performed to get quantitative insights into how cold CO_2 soil flux measurements are related to reservoir and fluid properties. Although the modeling is based on flux data measured at a specific geothermal site, the Acoculco caldera (Mexico), some general insights have been gained. Both the CO_2 fluxes at the surface and the depth at which CO_2 exsolves are highly sensitive to the dissolved CO_2 content of the deep fluid. If CO_2 mainly exsolves above the reservoir within a fracture zone, the surface CO_2 fluxes are not sensitive to the reservoir size but depend on the CO_2 dissolved content and the rock permeability. For gas exsolution below the top of the reservoir, surface CO_2 fluxes also depend on the gas saturation of the deep fluid as well as the reservoir size. The absence of thermal anomalies at the surface is mainly a consequence of the low enthalpy of CO_2. The heat carried by CO_2 is efficiently cooled down by heat conduction and to a certain extent by isoenthalpic volume expansion depending on the temperature gradient. Thermal anomalies occur at higher CO_2 fluxes ($>37{,}000\ g\ m^{-2}\ d^{-1}$) when the heat flux of the rising CO_2 is not balanced anymore. Finally, specific results are obtained for the Acoculco area (reservoir depth, CO_2 dissolved content, and gas saturation state).

1. Introduction

The monitoring of CO_2 degassing through soils has become a common practice during the last two decades for quantifying and characterizing the gas emissions in volcanic and geothermal areas [*Chiodini et al.*, 1998; *Bergfeld et al.*, 2001; *Lewicki and Oldenburg*, 2005; *Viveiros et al.*, 2010; *Mazot et al.*, 2011; *Peiffer et al.*, 2014]. A positive correlation is often observed between CO_2 soil degassing rate and soil temperature reflecting the upflow of a high enthalpy vapor and CO_2-rich fluid toward the surface [*Chiodini et al.*, 2005]. However, intense CO_2 degassing of magmatic origin without any soil temperature anomalies (i.e., cold CO_2) is also frequent. For example, at Mammoth Mountain (California), large areas with a degassing rate $\gg 1000\ g\ m^{-2}\ d^{-1}$ of cold CO_2 have been reported [*Sorey et al.*, 1998; *Gerlach et al.*, 2001; *Werner et al.*, 2014]. Other examples with important cold magmatic CO_2 degassing include Lakes Nyos and Monoun, Dieng Volcanic Plateau and Mount Gambier [*Giggenbach et al.*, 1991]. Conceptual models with a deep CO_2-rich gas pocket or gas reservoir were proposed to explain such cold discharge [*Giggenbach et al.*, 1991; *Sorey et al.*, 1998]. These models assume that below a certain depth hydrothermal systems are liquid dominated and contain a certain amount of dissolved magmatic gases. Then, upon fluid rising, the CO_2 solubility decreases due to the drop in temperature and pressure (CO_2 solubility may increase again when the temperature within the upflow area is below ~155°C). If the amount of CO_2 exceeds the maximum solubility, a free gas phase rich in CO_2 is formed. According to the proposed conceptual models [*Giggenbach et al.*, 1991; *Sorey et al.*, 1998], accumulation of CO_2 and the formation of a gas reservoir occur when a low permeability barrier, or caprock impedes further upflow of the formed gas phase. Such gas accumulations are manifested by high CO_2 fluxes at the surface if some of the CO_2 leaks through fractures. The tree kill event at Mammoth Mountain in the early 1990's was attributed to the leakage of a CO_2-rich gas pocket [*Sorey et al.*, 1998]. Because the CO_2 enthalpy is much lower than vapor enthalpy and CO_2 may have cooled down due to isoenthalpic volume expansion when it arrives at the surface [*Pruess*, 2008], such high CO_2 fluxes are not necessarily inducing a temperature anomaly as long as the CO_2 flow is not associated with significant water flow. The presence of a gas reservoir is also required to explain anomalous CO_2 fluxes in nonvolcanic areas from Italy [*Chiodini et al.*, 1999, 2010].

Although these conceptual models are well detailed, they do not give any quantitative insights into how the CO_2 and heat fluxes at the surface are related to reservoir and fluid properties (geometry, permeability, depth, temperature gradient, and content of dissolved CO_2) and how these fluxes evolve in time. Moreover, the mutual solubility of H_2O and CO_2 is not considered in these conceptual models even though this is an important mechanism controlling CO_2 migration via phase partitioning, especially in high-pressure reservoirs.

In this study, we use the numerical simulator TOUGH2 [*Pruess et al*., 1999], which has been applied in a large variety of numerical studies simulating volcanic and geothermal systems [*Chiodini et al*., 2003; *Kiryukhin and Yampolsky*, 2004; *McKenna and Blackwell*, 2004; *Hutnak et al*., 2009; *Rinaldi et al*., 2010, 2011, 2012; *Todesco et al*., 2010; *Fournier and Chardot*, 2012; *Viveiros et al*., 2014; *Wanner et al*., 2014]. Here we present simulations that are performed with the recently developed equation of state module ECO2N V2.0 accounting for properties of the CO_2-H_2O mixture over a wide range of conditions [*Pan et al*., 2014]. We model a hypothetical geothermal system based on the Acoculco caldera (Mexico), a promising geothermal area currently under exploration. This site is chosen because it has recently awakened the interest of the Mexican geothermal community due to its extraordinary high-temperature gradient of ~140°C/km [*López-Hernandez et al*., 2009; *Lorenzo Pulido et al*., 2011]. CO_2 flux soil measurements were recently performed there, and no soil temperature anomalies were detected [*Peiffer et al*., 2014]. The system has been described as a hidden or Hot Dry Rock (HDR) geothermal system due to the low permeability of the rocks as revealed by well cuttings, the lack of a well-developed water reservoir at depth, and the quasi-absence of thermal manifestations at the surface. This HDR system might be an ideal target for testing enhanced geothermal systems (EGS) due to the high-temperature gradient allowing drilling and stimulation activities at relatively shallow depths, as compared to other EGS sites (e.g., Soultz, 5 km).

The major objective of this study is to deduce, through numerical modeling, information on the physical-chemical conditions of a deep geothermal system from scarce measured data (such as temperature-pressure gradients, the rock composition, and CO_2 fluxes and temperature at the surface). In particular, in terms of a sensitivity analysis we performed a wide range of simulation scenarios involving various rock permeability conditions and fluid properties, reservoir and fractured zone geometries and different boundary conditions to reveal how these parameters affect CO_2 fluxes and temperature at the surface. Although the simulations and the input data are based on a particular system, the Acoculco caldera, the modeling methodology developed here and the obtained conclusions could be applied to describe the degassing dynamic of other geothermal systems, especially those lacking of superficial water-based thermal manifestations such as HDR or hidden geothermal systems.

2. Geology, Hydrothermal Activity and Conceptual Model

In this section, the main characteristics of the geology and hydrothermal activity of the Acoculco caldera are detailed in order to build an adequate conceptual model for the numerical simulations. The Acoculco caldera, located at 130 km northeast of Mexico City, belongs to the eastern part of the Trans Mexican Volcanic Belt (TMVB, Figure 1a). The caldera has a diameter of 18 km and lies within an older and wider caldera, the Tulancingo caldera. The system has not shown any volcanic activity for more than 0.2 Myr [*López-Hernandez et al*., 2009]. Two wells, EAC-1 and EAC-2, were drilled up to a maximum depth of ~2000 m by the Mexican Federal Electricity Company at the Los Azufres locality, which is within the Acoculco caldera. EAC-2 is located some 500 m northeast of EAC-1 [*Viggiano Guerra et al*., 2011, Figure 1a]. Although no water reservoir was observed during drilling, a few fluid entries were reported at shallow depth ($<$450 m), as well as at 1250 m and 1650 m depth. Temperature profiles monitored along the wells are mostly linear and suggest that conduction is the main heat transfer process and that the rock permeability is low (Figure 1b). The corresponding pressure profiles were qualitatively described as typical for hydrostatic conditions [*Viggiano Guerra et al*., 2011].

Through the analyses of well cuttings, the inferred low permeability of the system has been attributed to the high grade of hydrothermal alteration of the volcanic deposits (from 40 to 100% of secondary minerals) that constitutes the upper 800 m of the lithological column [*López-Hernandez et al*., 2009]. Metamorphic rocks of sedimentary origin, skarn, and marble, which formed due to a granitic intrusion, are exposed below this sequence. The actual granite is observed at the bottom of the wells (Figure 1b). The skarn and granite show limited alteration with about 10% of secondary minerals. It was inferred that the upper 800 m of altered

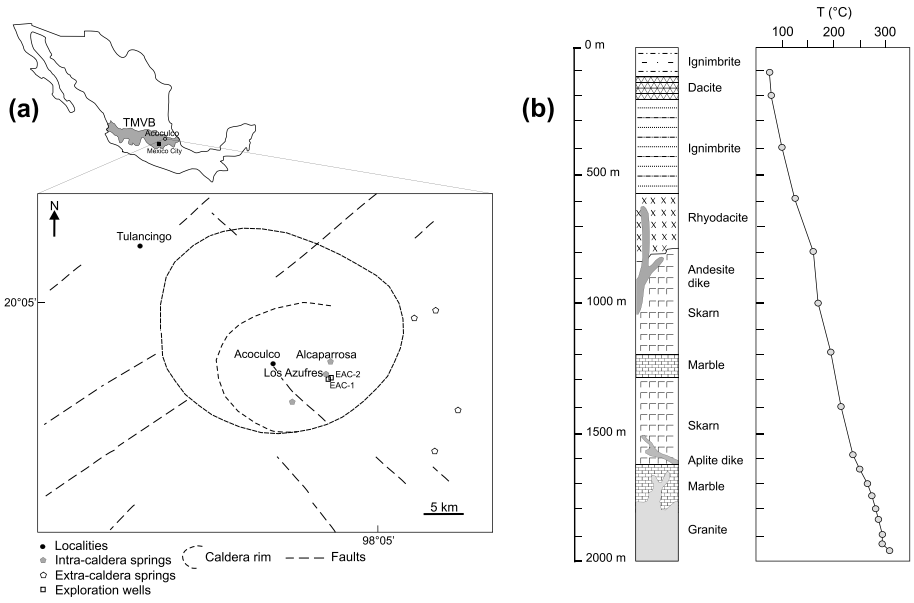

Figure 1. (a) Location and schematic representation of the Acoculco caldera illustrating the location of springs, main fault systems, the two exploration wells, and some localities. TMVB: Trans Mexican Volcanic Belt. (b) Lithologic column and temperature log from well EAC-1 (modified from *López-Hernandez et al*. [2009]).

rocks acts a caprock and impedes large fluid upflow to the surface [*López-Hernandez et al*., 2009]. In fact, within the caldera thermal manifestations are scarce and consist of a few bubbling springs and pools with close to ambient temperatures, and soil degassing and hydrothermally altered grounds. These manifestations are mainly occurring at two specific localities: Los Azufres and Alcaparrosa, which are separated by some 1500 m (Figure 1a). Intracaldera spring/pool waters show sulfate-calcium composition with acid to near-neutral pH (2.4–6.8) and $\delta^{18}O$-$\delta^{2}H$ composition close to the global meteoric water line. These waters thus probably emerge from shallow aquifers, water bodies, or stagnant pools of meteoric origin in which geothermal gases such as CO_2 and H_2S are dissolved. Outside the caldera, a few springs with near-neutral bicarbonate composition and temperatures up to 49°C were reported (Figure 1). Similar to the springs within the caldera, their chemical and isotopic water compositions indicate a meteoric origin. Nevertheless, chemical and isotopic compositions of bubbling gases (N_2/He, $^3He/^4He$, $\delta^{13}C$, and $\delta^{15}N$) reflect much deeper magmatic origin corresponding to a mixed signature between MORB and arc-type gases [*López-Hernandez et al*., 2009; *Peiffer et al*., 2014].

A campaign of preliminary soil multigas (CO_2-H_2S-CH_4) flux measurements was conducted recently within the caldera [*Peiffer et al*., 2014]. The two principal surveyed areas were Los Azufres and Alcaparrosa where 140 measurements were performed. Some additional 70 measurements were performed in surrounding areas characterized by highly altered rock outcrops [*Canet et al*., 2015]. Ninety five percent of measured CO_2 fluxes show low values (mean: 18 g m^{-2} d^{-1}, 90% interval of confidence (IC): 14–26 g m^{-2} d^{-1}) while the remaining 5% displayed higher values typical of hydrothermal/geothermal fluxes (mean: 5543 g m^{-2} d^{-1}, IC: 1906–27,713 g m^{-2} d^{-1}). Most of the high fluxes were measured at Alcaparrosa. Nevertheless, the presence of a large swamp area at Los Azufres impeded the measurement of fluxes over an area of 300 m by 30–80 m where localized gas bubbling can be observed. At Alcaparrosa, while the total surveyed area was about 11,000 m^2, the high fluxes were measured within a very localized and narrow area of ~ 1600 m^2, which probably reflects the trace of a local fault or a fracture zone with WNW-ESE orientation. The total CO_2 degassing rate of the two surveyed areas was estimated to 7 T d^{-1} (Alcaparrosa) and 18 T d^{-1} (Los Azufres), although for the latter it is probably a minimum because of the large swamp area as discussed above [*Peiffer et al*., 2014].

No surface temperature anomaly was observed within the whole surveyed area. The high fluxes show CO_2/H_2S and CO_2/CH_4 flux ratios (in g m^{-2} d^{-1}) similar to the CO_2/H_2S and CO_2/CH_4 mass ratios of directly sampled gas bubbles, suggesting that these fluxes correspond to gases transported by advection. The origin of the low flux data cannot be interpreted with confidence without ^{13}C isotopic data of the soil gases. They

might correspond to biogenic fluxes or reflect the transport of geothermal CO_2 by diffusion or by advection under low permeability conditions. Analyses of $\delta^{13}C$ in soil gases are required to discriminate the origin of low fluxes [*Peiffer et al*., 2014].

3. Gas Geothermometry

In this section gas geothermometry considerations for the Los Azufres and Alcaparrosa area are discussed to describe the temperature conditions at depth that are used to define the lower boundary conditions for our simulations. *Peiffer et al*. [2014] estimated gas equilibrium temperatures from the CH_4/CO_2 and CO_2/Ar concentration ratios using the following gas geothermometers [*Giggenbach*, 1991, 1997]:

$$\log\left(X_{CO_2}/X_{Ar}\right) = 0.0277T - 7.53 + [2048/(T + 273.15)] \quad (1)$$

$$T = \{4625/[10.4 + \log(X_{CH_4}/X_{CO_2})]\} - 273.15 \quad (2)$$

where X_i refers to the molar concentration in the gas sample, in this case the bubbling gas. T is the temperature in °C.

The CO_2/Ar geothermometer depicted in equation (1) assumes that the originally dissolved CO_2 content of a fluid is buffered by primary (Ca-Al silicates and feldspars) and secondary minerals (calcite and clays), while the Ar content corresponds to the content of air-saturated groundwater of meteoric origin. Equation (2) refers to the CH_4/CO_2 geothermometer, which assumes that the equilibrium of both gases dissolved into water is controlled by the FeO-$FeO_{1.5}$ redox buffer (fayalite-hematite).

Using the CO_2/Ar and CH_4/CO_2 gas ratios measured at Los Azufres and Alcaparrosa in conjunction with equations (1) and (2), a mean temperature of 306°C with a standard deviation of 58°C is obtained [*Peiffer et al*., 2014]. It should be noted that this calculation considers that the measured gas ratios correspond to the original gas ratios in a dissolved state (i.e., single-phase conditions). Therefore, the large standard deviation may reflect some degree of vapor-liquid separation, as proposed by *Chiodini et al*. [1996] to explain the chemistry of low-temperature gases close to Mount Etna. If the measured CO_2/Ar and CH_4/CO_2 ratios are considered to be the result of a previously exsolved vapor/gas phase being at equilibrium with the deep original liquid (i.e., two-phase conditions), the temperature of equilibrium of the original liquid phase become higher than the gas geothermometry calculations assuming single-phase conditions such as those discussed as follows.

For a two-phase system, the CO_2/Ar and CH_4/CO_2 ratios in the gas phase (at equilibrium with the liquid phase) are linked to the dissolved gas ratios by the Henry constants for each gas:

$$P_{CO_2}/P_{Ar} = \left(K_{h,CO_2}/K_{h,Ar}\right)\left(X_{CO_2}/X_{Ar}\right) \quad (3)$$

$$P_{CH_4}/P_{CO_2} = \left(K_{h,CH_4}/K_{h,CO_2}\right)\left(X_{CH_4}/X_{CO_2}\right) \quad (4)$$

with P being the partial pressure (atm) and K_h referring to the Henry constants for each gas in atm/mol fraction, which are taken from *Plyasunov and Shock* [2003].

Using equations (3) and (4), the gas ratios in the gas phase at the liquid-gas equilibrium can be obtained for various temperatures of separation. Gas geothermometers (equations (1) and (2)) are then applied using these gas ratios to assess the effect of gas phase separation on geothermometry estimations.

Specific dissolved gas ratios ($X_{CH4}/X_{CO2,\ liq}$: 0.00467, 0.00105; $X_{CO2}/X_{Ar,\ liq}$: 22785, 282841) yield CH_4/CO_2 and CO_2/Ar geothermometer estimates of 300°C and 350°C ($T_{CH4/CO2,\ 1phase}/T_{CO2/Ar,\ 1phase}$, Table 1), approximately representing the mean and maximum temperature originally estimated using equations (1) and (2) [*Peiffer et al*., 2014]. Temperature estimates obtained using a separation temperature identical to the liquid temperature (300°C or 350°C) are ~30–40°C lower than the initial liquid temperature estimate ($T_{CH4/CO2,\ 2phase}$, $T_{CO2/Ar,\ 2phase}$, Table 1). For lower separation temperature (e.g., 200°C), the temperature estimates are ~40–60°C lower than the corresponding liquid temperature estimation. The temperature estimates obtained with a separation temperature of 65°C (Table 1) are even lower and will be discussed later together with the simulation results.

It should be noted that these geothermometry calculations are based on Henry's law and do not take into account the solubility of CH_4 and Ar within a free (maybe supercritical) CO_2 phase. Furthermore, the gas phase is considered to be totally separated from the deep liquid. If the sampled gas is a mixture of the deep

Table 1. Gas Geothermometer Calculations Showing the Impact of Gas Phase Separation on Temperature Estimates[a]

$X_{CH4}/X_{CO2,\ liq}$ (mol fraction)	$X_{CO2}/X_{Ar,\ liq}$ (mol fraction)	$T_{CH4/CO2,\ 1phase}$ / $T_{CO2/Ar,\ 1phase}$ (°C)	T_{sep} (°C)	$K_{h,CO2}$ (atm/mol fraction)	$K_{h,CH4}$ (atm/mol fraction)	$K_{h,Ar}$ (atm/mol fraction)	$X_{CH4}/X_{CO2,\ gas}$ (mol fraction)	$X_{CO2}/X_{Ar,\ gas}$ (mol fraction)	$T_{CH4/CO2,\ 2phase}$ (°C)	$T_{CO2/Ar,\ 2phase}$ (°C)
0.00467	22,785	300	300	3,597	13,065	16,665	0.0170	4,918	263	269
			250	4,518	21,192	24,460	0.0219	4,209	256	266
			200	5,456	34,238	36,350	0.0293	3,420	248	261
			65[b]	3,581	60,064	58,314	0.0784	1,399	224	242
0.00105	282,841	350	350	2,757	7,993	11,432	0.0031	68,208	313	322
			300	3,597	13,065	16,665	0.0038	61,054	306	320
			250	4,518	21,192	24,460	0.0049	52,244	298	317
			200	5,456	34,238	36,350	0.0066	42,450	290	313

[a]Given ratios of dissolved gas concentrations ($X_{CH4}/X_{CO2,\ liq}$ and $X_{CO2}/X_{Ar,\ liq}$) are chosen to mimic the mean (300°C) and maximum temperatures (350°C) given by gas geothermometers applied to Acoculco gases. These temperatures ($T_{CH4/CO2,\ 1\ phase}/T_{CO2/Ar,\ 1phase}$) assume that the gases were equilibrated in a dissolved state within a single-phase liquid. Considering the Henry's constant ($K_{h,i}$) for each gas species at different temperatures of phase separation (T_{sep}), the gas ratios in the gas phase at equilibrium with the liquid phase ($X_{CH4}/X_{CO2,\ gas}$ and $X_{CO2}/X_{Ar,\ gas}$) and the corresponding gas geothermometers ($T_{CH4/CO2,\ 2phase}$ and $T_{CO2/Ar,\ 2phase}$) are computed. Calculations are based on equations (1) to (4).

[b]The T_{sep} corresponds to the temperature at a depth of 300 m from which 50% of the CO2-rich phase exsolves in simulation #A.a.1.

liquid and a fraction (y) of equilibrated vapor/gas, then the concentration of each gas species in the total discharge ($X_{d,i}$) should be calculated as proposed by *Giggenbach* [1980]:

$$X_{d,i} = X_{l,i}(1-y) + X_{v,i}y \tag{5}$$

where $X_{l,i}$ and $X_{v,i}$ stands for the gas content in the equilibrated liquid phase and in the equilibrated gas phase, respectively.

Based on equation (5), temperature estimates presented in Table 1 assume a gas phase entirely separated from the original liquid ($y=1$). If y is <1, the temperature estimate would be between the original liquid temperature (300°C or 350°C) and the "$y=1$" geothermometer estimate ($T_{CH4/CO2,\ 2phase}$ or $T_{CO2/Ar,\ 2\ phase}$) as listed in Table 1.

In summary, our gas phase separation calculations confirm that the large temperature range (306 ± 58°C) obtained by applying gas geothermometers to the Los Azufres and Alcaparrosa gases (equations (1) and (2)) can be explained by gas phase separation at different temperatures (minimum: 200°C, maximum: 350°C) and/or by different mixtures of original liquid and vapor phase (y: 0–1) in the total gas discharge. This temperature range, where both liquid and gas phase can coexist, will be considered in the next section for discussing the possible depth of gas exsolution and setting diverse types of conditions at the lower boundary of the simulation domain.

4. Numerical Model Settings

4.1. TOUGH2-ECO2N V2.0

Numerical simulations are performed with the multipurpose TOUGH2 simulator, which solves heat transfer and fluid flow equations in porous media [*Pruess et al*., 1999]. The equation of state (EOS) module ECO2N V2.0 [*Pan et al*., 2014] is used because of its capacity to simulate multicomponent (H_2O and CO_2) two-phase flow at high temperatures (up to 300°C) and pressures (up to 600 bar), well beyond the critical point for CO_2 (31.04°C, 73.82 bar). ECO2N V2.0 considers the mutual solubility model of H_2O and CO_2 in H_2O-rich aqueous and CO_2-rich gas phases as a function of temperature, pressure, and salinity, using the correlations developed by *Spycher et al*. [2003] and *Spycher and Pruess* [2005, 2010]. In our simulations, the sensitivity on salinity variations is not explored. Nevertheless, we use ECO2N because other EOS modules such as EOS2 do not have the capability to treat the mutual solubility of CO_2 and H_2O. More details on the ECO2N module can be found in *Pan et al*. [2014].

4.2. Mesh Dimensions and Geometry

CO_2 flux measurements for the Alcaparrosa area are better constrained than the ones for Los Azufres. Accordingly, the numerical simulations aim at reproducing the range of high CO_2 fluxes data (1906–27,713 g m^{-2} d^{-1} of CO_2) measured in the Alcaparrosa area. Because the two areas are separated by about 1500 m and no soil gas flux

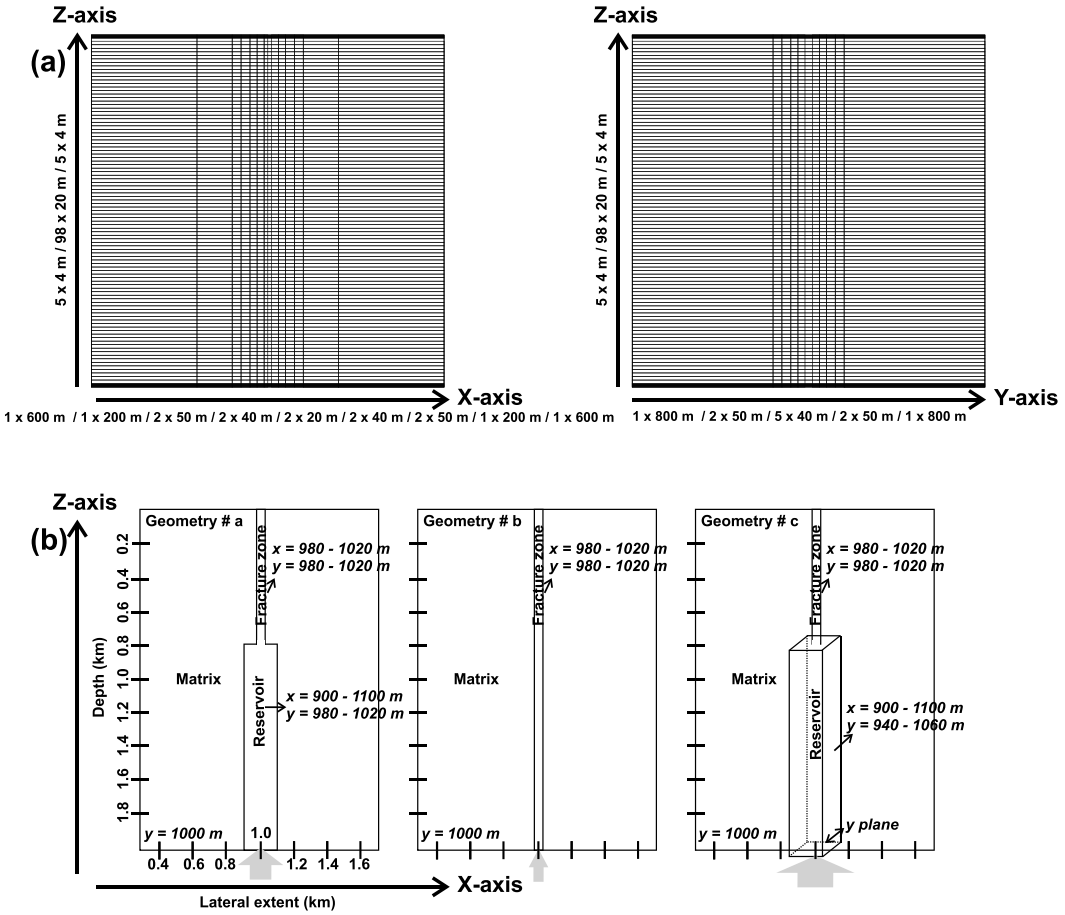

Figure 2. (a) Schematic representation of the 3-D mesh discretized in 16,632 blocks. Also shown are the number of blocks and their extension in the three axes. (b) View of the *xz* plane at $y = 1000$ m with the location of the three model domains: reservoir, fracture zone, and matrix. Grey arrows symbolize the fluid injection over the reservoir or fracture zone at the bottom model boundary. Because the conditions close to the lateral model boundaries do not vary between simulations, the lateral extension in the *x* axis is deliberately shortened to the domain between 0.3 and 1.7 km for graphical representation. The following figures will be presented in the same way.

anomalies have been reported in between them, the simulations will focus on the vertical migration of geothermal gases from depth to the surface, without considering lateral migration.

The mesh used to simulate the Alcaparrosa area is three dimensional, and the dimensions are $x = 2000$ m, $y = 2000$ m, and z (depth) $= 2000$ m, and it is discretized into 16,632 grid blocks with variable extents (Figure 2a).

The presence of a liquid or gas reservoir at depth was not revealed during drilling of wells EAC-1 and EAC-2. However, due to the small distance between the two wells (500 m), the presence of a small-scale reservoir at depth cannot be excluded. To investigate the likelihood of having such a reservoir, simulations are performed for three different reservoir geometries (geometry #a–c, Figure 2b). For each geometry the model is divided into three domains for which different permeability is assigned: (i) reservoir domain, (ii) fracture zone domain, and (iii) matrix domain. The permeability specified for the different domains are listed in Table 2 for each model run.

Geometry #a simulates a hypothetical deep reservoir which extends vertically (*z* axis) from a depth of 800 m to the bottom of the mesh ($z = 2000$ m) and has a lateral extent from $x = 900$–1100 m and $y = 980$–1020 m (Figure 2b). The upper limit is based on the observation that the upper 800 m of the lithological column at Acoculco are highly altered. The marble-skarn-granite basement shows less alteration and is thus more susceptible to host a reservoir, whose permeability, if any, could be controlled by fractures. The reservoir is connected to the surface through the fracture zone domain defined at $x = 980$–1020 m, $y = 980$–1020 m, and $z = 0$–800 m. The intersection area between the fracture zone domain and a horizontal plane (e.g., ground surface) is set to 40×40 m

AGU Journal of Geophysical Research: Solid Earth

10.1002/2015JB012258

Table 2. Initial Conditions Specified for the Various Model Runs and Corresponding Results Obtained in the Upper Part of the Fracture Zone After 10,000 Years of Simulation[a]

	Scenario	Geometry	Simulation #	overP (%)	X_{CO2} (mol %)	Sg_i	k Reservoir (m^2)	k Fracture (m^2)	k Matrix (m^2)	T (°C)	Sg	$X_{CO2,g}$ (mol %)	$F_{CO2,g}$ ($g\,m^{-2}\,d^{-1}$)	F_{liq} ($kg\,s^{-1}$)
Single stage simulations	Shallow exsolution (#A)	a	A.a.1	10	1.8	0	5×10^{-15}	5×10^{-15}	1×10^{-20}	25.65	0.16	98.11	15	0.004
			A.a.1b	10	2.2	0	5×10^{-15}	5×10^{-15}	1×10^{-20}	25.65	0.17	98.11	18	0.003
			A.a.2	10	1.8	0	5×10^{-15}	5×10^{-15}	1×10^{-18}	25.65	0.16	98.07	14	0.003
			A.a.3	10	1.8	0	5×10^{-16}	5×10^{-16}	1×10^{-20}	25.56	0.15	98.11	1	0.0004
			A.a.4	10	1.8	0	1×10^{-14}	1×10^{-14}	1×10^{-20}	25.78	0.16	98.10	32	0.007
			A.a.5	10	1.8	0	5×10^{-14}	5×10^{-14}	1×10^{-20}	28.19	0.17	97.89	198	0.043
			A.a.6	10	1.8	0	5×10^{-15}	1×10^{-14}	1×10^{-20}	25.76	0.16	98.08	30	0.007
			A.a.7	10	1.8	0	5×10^{-15}	1×10^{-13}	1×10^{-20}	27.24	0.15	97.64	147	0.032
			A.a.8	10	1.8	0	1×10^{-14}	5×10^{-14}	1×10^{-20}	27.15	0.16	97.88	143	0.031
			A.a.9	10	1.8	0	1×10^{-14}	1×10^{-13}	1×10^{-20}	29.17	0.16	97.52	238	0.052
		a/half F	A.a.9b	10	1.8	0	1×10^{-14}	1×10^{-13}	1×10^{-20}	27.99	0.16	97.73	265	0.058
		b	A.b.1	10	1.8	0	/	5×10^{-15}	1×10^{-20}	25.64	0.16	98.03	12	0.003
			A.b.2	10	1.8	0	/	1×10^{-14}	1×10^{-20}	25.73	0.16	98.03	27	0.006
			A.b.3	10	1.8	0	/	5×10^{-14}	1×10^{-20}	27.50	0.16	97.89	163	0.035
			A.b.4	10	1.8	0	/	1×10^{-13}	1×10^{-20}	33.45	0.17	97.12	405	0.087
			A.b.5	5	1.8	0	/	1×10^{-13}	1×10^{-20}	28.24	0.16	97.58	198	0.043
		c	A.c.1	10	1.8	0	5×10^{-15}	5×10^{-15}	1×10^{-20}	25.66	0.16	98.12	15	0.004
			A.c.2	10	1.8	0	1×10^{-14}	1×10^{-14}	1×10^{-20}	25.78	0.16	98.12	33	0.007
			A.c.3	10	1.8	0	5×10^{-14}	5×10^{-14}	1×10^{-20}	28.18	0.17	97.91	200	0.044
	Deep exsolution (#B)	a	B.a.1	0	1.95	0.41	5×10^{-15}	5×10^{-15}	1×10^{-20}	25.34	0.51	98.53	1,634	0.00003
			B.a.2	5	2.15	0.37	5×10^{-15}	5×10^{-15}	1×10^{-20}	25.33	0.45	98.73	1,717	0.0002
			B.a.3	10	2.34	0.34	5×10^{-15}	5×10^{-15}	1×10^{-20}	25.32	0.42	98.84	1,793	0.0004
			B.a.4	0	1.95	0.41	1×10^{-14}	1×10^{-14}	1×10^{-20}	25.15	0.49	98.60	3,244	0.0001
			B.a.5	0	1.95	0.41	5×10^{-14}	5×10^{-14}	1×10^{-20}	24.56	0.42	98.85	16,115	0.004
			B.a.5b	0	1.95	0.101	5×10^{-14}	5×10^{-14}	1×10^{-20}	25.49	0.26	97.67	433	0.00002
			B.a.6	0	1.95	0.41	5×10^{-15}	1×10^{-14}	1×10^{-20}	25.35	0.45	98.37	1,641	0.0002
			B.a.7	0	1.95	0.41	5×10^{-15}	1×10^{-13}	1×10^{-20}	25.38	0.31	97.81	1,876	0.0026
			B.a.8	0	1.95	0.41	1×10^{-14}	5×10^{-14}	1×10^{-20}	25.20	0.37	98.21	3,475	0.0025
			B.a.9	0	1.95	0.41	1×10^{-14}	1×10^{-13}	1×10^{-20}	25.26	0.34	98.02	3,709	0.0048
		b	B.b.1	0	1.95	0.41	/	5×10^{-15}	1×10^{-20}	25.51	0.38	98.12	345	0.0002
			B.b.2	0	1.95	0.41	/	1×10^{-14}	1×10^{-20}	25.47	0.38	98.14	690	0.0004
			B.b.3	0	1.95	0.41	/	5×10^{-14}	1×10^{-20}	25.23	0.36	98.27	3,542	0.0036
			B.b.4	0	1.95	0.41	/	1×10^{-13}	1×10^{-20}	25.43	0.34	98.38	7,573	0.013
		c	B.c.1	0	1.95	0.41	5×10^{-15}	5×10^{-15}	1×10^{-20}	24.71	0.43	99.23	4,892	0.0007
			B.c.2	0	1.95	0.41	1×10^{-14}	1×10^{-14}	1×10^{-20}	23.85	0.42	99.29	9,698	0.0017
			B.c.3	0	1.95	0.41	5×10^{-14}	5×10^{-14}	1×10^{-20}	42.45	0.36	98.25	37,461	0.038
Three stages simulations	#A	a	A.a.10	10	1.8	0	5×10^{-15}	1×10^{-13}	1×10^{-20}	27.24	0.15	97.64	147	0.032
	#B	a	B.a.10	10	2.34	0.34	5×10^{-15}	5×10^{-15}	1×10^{-20}	25.32	0.42	98.84	1,801	0.0004
Two stages simulations	#A	a	A.a.11	10	1.8	0	5×10^{-15}	1×10^{-13}	1×10^{-20}	27.23	0.15	97.64	147	0.032
	#B	a	B.a.11	10	2.34	0.34	5×10^{-15}	5×10^{-15}	1×10^{-20}	25.32	0.42	98.84	1,801	0.0004

[a]Simulations' conditions: overP: overpressure; X_{CO2} and Sg_i: CO_2 dissolved content (mol%) and gas saturation of the injection fluid, respectively; k: permeability. Results: temperature (T); gas saturation (Sg); CO_2 content in the gas phase ($X_{CO2,g}$, mol%); CO_2 flux (F_{CO2}, $g\,m^{-2}\,d^{-1}$) and liquid flux (F_{liq}, $kg\,s^{-1}$). "half F" stands for half fracture. For all simulations #B, X_{CO2} represents the CO_2 solubility limit. Before internal conversion by ECO2N, the CO_2 content given as input for the injection fluid is 5 mol % for all simulations #B, except #B.a.5b, for which a value of 2.5 mol % is defined. Except simulations #A.a.10, #B.a.10, #A.a.11, and #B.a.11, all simulations are single stage simulations.

corresponding to the dimensions of the high degassing area at Alcaparrosa. For geometry #a, the reservoir is defined within the *xz* plane only. Therefore, the simulations are in this case essentially 2-D, although heat transfer by conduction occurs in the rest of the mesh and efficiently cools down the rising fluid. For this reason, simulations results will be represented in 2-D, within the reservoir-fault plane (*xz* plane, $y = 1000$ m).

Geometry #b simulates a no-reservoir scenario to test whether it is possible to reproduce the CO_2 fluxes measured at the surface without a gas reservoir within the upper 2 km. To do so, no reservoir domain is specified and the fracture zone domain is extended along the entire *z* axis (Figure 2b).

Geometry #c simulates the presence of a reservoir that is 3 times larger (volume = 288×10^5 m^3) than the one considered in geometry #a (volume = 96×10^5 m^3). Accordingly, the reservoir is now specified for a 3-D domain ($x = 900$–1100 m, $y = 940$–1060 m) also in terms of the computational mesh ($x \times y$ grid blocks). For graphical representation ease, results from geometry #c simulations are also presented in 2-D (*xz* plane, $y = 1000$ m). The reservoir geometry is deliberately chosen as a perfect cuboid due to the lack of information about the real geometry. As the maximum volume of the reservoir is small (geometry #c), we believe that this is a reasonable approximation. In fact, owing to its limited volume, the modeled reservoir is probably closer to an "extended fracture zone" at depth. Nevertheless, the term "reservoir" will be used throughout the paper because the present modeling approach can be easily applied to larger reservoir as well.

For all three geometries, the reservoir and fracture zone domains are surrounded by the matrix domain representing the low permeability section of the mesh, where fluid flow is limited and conduction is the main heat transfer mechanism. The part of the matrix overlying the reservoir ($z < 800$ m) is further referred to as caprock.

4.3. Initial and Boundary Conditions

A hydrostatic pressure gradient is defined as initial condition together with a conductive thermal gradient of 138°C/km, which is close to the temperature profile measured within well EAC-1 (Figure 1b). The mesh is initially fully saturated with pure water. Fixed boundary conditions of temperature and pressure are assigned at the surface (1 bar, 25°C) and at the bottom of the mesh (hydrostatic $P = 176.3$ bar, 300°C). The temperature limit cannot be increased due to the modeling capacity of ECO2N V2.0. Lateral and vertical boundaries are impermeable to heat and fluid flow while fluid and heat flow is occurring across the bottom and upper boundaries. The lower boundary conditions beneath the reservoir (geometry #a and #c) or fracture zone (geometry #b) domains vary with simulation scenarios which will be described below.

4.4. Rock Properties, Relative Permeabilities, and Capillary Pressure

The porosity is set to 0.1 for all the three domains, while a large range of permeability values from 5×10^{-16} to 1×10^{-13} m^2 is chosen for the reservoir as well as for the fracture zone domain, and low values of 1×10^{-20} to 1×10^{-18} m^2 are considered for the matrix domain. These permeability values are typically reported in geothermal systems [*Manning and Ingebritsen*, 1999], while the porosity is chosen from other modeling studies [*Todesco et al*., 2010; *Fournier and Chardot*, 2012] due to the lack of porosity measurements at this site. Changing the porosity of the reservoir and fracture zone would affect the temporal evolution of the different modeled parameters (e.g., gas saturation, *T*, and *P*), but steady state solutions would be similar regardless of the porosity. Owing to the low permeability of the matrix, fluid flow throughout this domain is restricted, and therefore, assigning a different value of porosity would have limited impact on the simulation results.

Thermal conductivity is set to 2.5 W m^{-1} K^{-1} for the whole mesh, while values of 2600 kg m^{-3} and 1000 J kg^{-1} K^{-1} are assigned for the rock density and specific heat, respectively. Since no direct measurements of these rock properties are available at Acoculco, the specified values are taken from *Todesco et al*. [2010] and *Wanner et al*. [2014]. The relative permeability for water and gas phases is computed according to the van Genuchten-Mualem model [*Mualem*, 1976; *van Genuchten*, 1980], using irreducible saturation values of 0.3 and 0.05 for the liquid and gas phase, respectively, and a value of 0.457 for the *m* exponent. Capillary pressure is computed from the *van Genuchten* [1980] function and reaches a maximum of 1 bar at the liquid irreducible saturation value.

4.5. Simulation Scenarios

At Acoculco, direct observations of the physical-chemical conditions at depth are scarce and consist of temperature-pressure gradients and rock types only. Accordingly, a large range of conditions is explored

to get more insights into the degassing dynamic. The idea is to track the migration of a CO_2-rich fluid that flows from the bottom of the reservoir (geometry #a and #c) or the fracture zone (in the no-reservoir scenario, geometry #b) toward the top of the fracture zone. The evolution of the free gas phase will be monitored and compared with measured CO_2 fluxes at the surface.

There are two ways to induce flow with TOUGH2. The first one consists in assigning a fixed or variable injection rate of a given component (H_2O and/or CO_2) to one or several blocks from which flow is initiated. The second approach relies on the fact that the TOUGH2 simulator is based on Darcy's law. Fluid flow can therefore be induced by increasing the pressure gradient and/or reducing the fluid density (i.e., increasing the effective driving force) at the model boundaries. In this study, the later option is chosen. Because the fluid flow occurs from the bottom of the reservoir (or from the fracture bottom in geometry #b; arrows in Figure 2b) toward the upper part of the fracture zone, we will further use the term "injection fluid" to refer to the fluid that flows from this specific section of the lower boundary into the model domain. One advantage of using a fixed pressure boundary condition is that it is possible to simulate a sealing event in which the fluid flow rate within the domain will be gradually decreasing with time in response to the *P* gradient evolution within the sealed system. Since the dynamic of such a decrease is unknown prior to performing simulations, the variable injection rate method is not suitable. Another advantage of the constant pressure option is that the CO_2 content of the injection fluid can be easily assigned by specifying a specific CO_2 mass fraction, rather than having to adjust the H_2O and CO_2 injection rates using the variable injection rate option. This is particularly useful because it is straightforward to compare a certain input value with the CO_2 solubility in water at a given *P* and *T* [*Spycher and Pruess*, 2005, 2010]. Moreover, one of the few quantitative model discussing the formation of CO_2-rich reservoir is formulated in terms of mol % units, which can be simply converted to CO_2 mass fractions [*Giggenbach et al*., 1991]. Choosing the fixed pressure option thus facilitates the comparison of results derived from different models. The mol % units will be used in this study to discuss the CO_2 content of the injection fluid.

The fixed temperature defined at the lower model boundary (300°C = injection temperature) is within the temperature range estimated using the CO_2/Ar and CO_2/CH_4 geothermometers for various gas phase separation assumptions (Table 1). Based on these geothermometry considerations, the fluid injected at the base of the mesh (2 km depth, 300°C) could either be a single-phase liquid representing a condensed magmatic vapor (i.e., water) with dissolved gases or a two-phase mixture between a liquid (i.e., liquid water with dissolved CO_2) and a CO_2-rich phase. This CO_2-rich phase may be gaseous or supercritical and contains dissolved H_2O [*Spycher et al*., 2003; *Spycher and Pruess*, 2005, 2010; *Pan et al*., 2014]. The term "gas phase" will be further used to refer to this CO_2-rich phase.

To consider both possibilities, we performed two types of simulations. Simulations #A or "shallow exsolution" simulations are performed by injecting a liquid phase with a certain amount of dissolved CO_2 and are meant to generate CO_2 exsolution within the model domain ($z < 2000$ m). On the opposite, simulations #B, called "deep exsolution" simulations, are performed by injecting a CO_2-rich phase produced by CO_2 exsolution at a greater depth, below our model domain ($z > 2000$ m). For both scenarios the fluid is injected over the whole surface area corresponding to the bottom of the reservoir or fracture zone domain (arrows in Figure 2b).

For the shallow exsolution scenarios, an overpressure (i.e., over the regular hydrostatic pressure) is specified for the lower boundary blocks where fluid injection occurs. This overpressure is needed for inducing upflow because of the simplicity of the model domain which has no surface topography allowing at depth a natural overpressure above the hydrostatic pressure [*Wanner et al*., 2014]. A value of 10% above the regular hydrostatic pressure is chosen for all #A simulations, except for simulation #A.b.5 for which a value of 5% is set to evaluate the impact on the flow rate. By specifying an overpressure of 5–10% we basically assume that upflow is driven by a pressure head within an arbitrary topographic high outside of our model domain. Accordingly, we do not postulate that such overpressured conditions are actually occurring at Acoculco. Nevertheless, the specified magnitude of overpressure was reported for a wide series of geothermal field sites [*Serpen and Niyazi*, 2005].

When injecting a CO_2-rich phase (deep exsolution simulations #B), buoyancy force induces upflow of the gas phase, and there is no need to specify a pressure above hydrostatic. Because no overpressure is used in simulations #B, no liquid will be injected in the reservoir-fracture domains. Nevertheless, several

simulations (e.g., #B.a.2 and #B.a.3) are repeated with a given overpressure to evaluate the sensitivity of the results to this parameter.

The maximum CO_2 solubility at the pressure-temperature (*P-T*) conditions of injection for the shallow exsolution (#A) simulations (176 + 10% = 193 bar, 300°C) is 2.34 mol % [*Spycher and Pruess*, 2010]. Accordingly, a value of 1.8 mol %, which is below the maximum CO_2 solubility, is specified for the shallow exsolution simulations (#A). This specification yields a CO_2 partial pressure of 67 bar. Several simulations #A are performed using the three types of reservoir geometry and different permeability values (#A.a.1 to #A.c.3, Table 2). Simulation #A.a.1b is the only shallow exsolution simulation with a different dissolved CO_2 content of 2.2 mol %. It is performed to test a scenario where the dissolved content is close to the CO_2 solubility limit while the other parameters (geometry and permeability) remained the same as for simulation #A.a.1 to allow a direct comparison. An additional simulation (#A.a.9b) with unique geometry is performed to test the CO_2 flux sensitivity to the surface area of the fracture zone domain. For this purpose, the same settings as for simulation #A.a.9 (geometry #a, $k_{res} = 1 \times 10^{-14}$ m^2, $k_{fracture} = 1 \times 10^{-13}$ m^2, 1.8 mol % CO_2) are used but this time with a reduced fracture zone. To do so, the lateral extent of the fracture zone is reduced to 20 m × 40 m (compared to 40 m × 40 m in all other simulations).

ECO2N internally checks if the input dissolved CO_2 content is within the range for single-phase (aqueous) conditions, and if it is not the case it automatically computes the corresponding gas saturation (i.e., the fraction of the CO_2-rich phase) from the phase equilibrium constraint [*Pan et al*., 2014]. For the deep exsolution simulations (#B), a CO_2 content of 5 mol % is set for the injection fluid. This value is deliberately higher than the solubility limit at 176 bar (no overpressure) and 300°C (1.95 mol %) and is chosen because it yields CO_2 fluxes at the surface that are highly contrasting the ones obtained from the shallow exsolution simulations (#A). ECO2N internally converts this concentration to a gas saturation (= CO_2-rich phase) of 0.41 and corresponding P_{H2O} and P_{CO2} of 103 and 73 bar, respectively [*Spycher and Pruess*, 2010]. For simulations #B.a.2 and #B.a.3, the CO_2 solubility limit and the gas saturation of the injection fluid are slightly different because of the specified overpressure (Table 2).

Subsequently, the sensitivity of the deep exsolution simulations (#B) to the permeability of the three domains and the geometry is evaluated (#B.a.1 to #B.c.3, Table 2). Simulation #B.a.5b is a deep exsolution simulation that is performed with a different injection gas saturation of 0.101 (2.5 mol % before internal conversion) for comparison with other simulations #B. This simulation has the same geometry and permeability characteristics than #B.a.5. All simulations are run for a period of 10,000 years after which the simulated surface CO_2 fluxes reach close to steady state values.

Finally, a transient sealing of the fracture zone is simulated under shallow (#A) and deep CO_2 exsolution (#B) conditions. These simulations aim at reproducing a sealing event of the fracture zone in order to model gas accumulation within a sealed reservoir. The simulated sealing event represents a scenario where the precipitation of authigenic minerals (e.g., silica, calcite, and clays) within the fracture zone leads to a self-sealing of the reservoir by decreasing the permeability of the fracture zone. After the sealing event, the fracture zone is reopened to simulate a permeability enhancement possibly triggered by a seismic event. Therefore, the sealing simulations also allow to understand the surface degassing dynamic after such an event and to estimate the time needed for the system to recover to steady state conditions. The simulations are performed with (#A.a.10 and #B.a.10) or without (#A.a.11 and #B.a.11) initial conditions inherited at the end of specific simulations #A and #B to simulate a period of degassing through a fracture zone prior to the sealing event, or a system initially sealed (three or two stages simulations as denoted in Table 2). A 10% overpressure is applied to the injection area for simulations #B.a.10 and #B.a.11 to allow a straightforward comparison with simulations #A.a.10 and #A.a.11. Owing to the higher pressure, the gas saturation of the injection fluid is reduced to 0.34 for these simulations #B while the CO_2 dissolved content before internal ECO2N conversion remains the same (5 mol %).

5. Results

5.1. Shallow Exsolution Simulations (#A)

5.1.1. Geometry #a

Temperature (*T*), gas saturation (Sg), CO_2 concentration in the gas phase (X_{CO2g}, mol %), CO_2 gas flux (F_{CO2}, g m^{-2} d^{-1}), and liquid flux (F_{liq}, kg s^{-1}) obtained at the top of the fracture zone (just below the surface) after

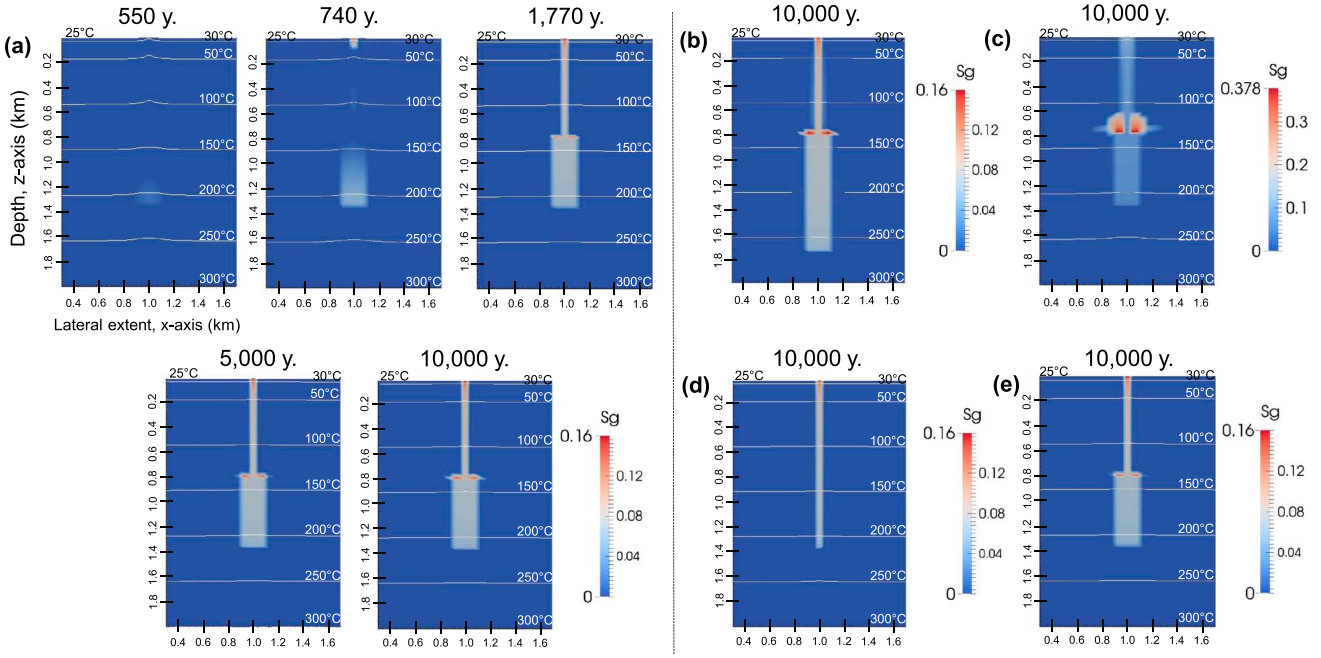

Figure 3. (a) Evolution of the gas saturation (Sg) profile within the plane of injection, at different times of simulation #A.a.1. (b–e) Sg profiles at 10,000 years in simulations #A.a.1b, #A.a.2, #A.b.1, and #A.c.1, respectively.

a simulation time of 10,000 years are listed in Table 2. For simulation #A.a.1 ($k_{fracture} = k_{reservoir} = 5 \times 10^{-15}$ m^2, $k_{matrix} = 1 \times 10^{-20}$ m^2) the temporal evolution of the gas saturation within the injection plane is illustrated in Figure 3a. The figure shows that after 500 years of simulation, a CO_2-rich gas phase (Sg > 0) appears between depths of 1150 and 1400 m within the reservoir. Starting at 740 years, exsolution also occurs within the upper part of the fracture zone, right below the surface. Subsequently, the two CO_2 exsolution zones are increasing and merge into one at 1770 years. From 5000 years to the end of the simulation, the simulated CO_2 flux at the surface is steady with a value of 0.28×10^{-3} kg s^{-1} or 15 g m^{-2} d^{-1} (Table 2). The maximum Sg value (0.16) is reached below the caprock and within the upper part of the fracture zone. Moreover, it is observed that some of the CO_2-rich phase spreads laterally within the low permeability matrix below the caprock. The maximum depth where exsolution occurs is 1350 m (550 m below the caprock) reflecting the depth where the maximum CO_2 solubility is exceeded due to the pressure drop during upflow. During the simulation, the vertical temperature and pressure profiles remains fairly similar to initial conditions (Figure 3a). The CO_2 and H_2O partial pressure profiles at steady state within the fracture-reservoir plane show that when the gas phase starts to exsolve at 1400 m depth, it consists of approximately 80 mol % CO_2 and 20 mol % H_2O (Figure 4). At a depth of 800 m (i.e., bottom of the fracture zone domain), the gas phase consists of 95% CO_2, while at the surface it is almost pure CO_2 (98%).

The maximum depth of CO_2 exsolution increased to 1750 m when the dissolved CO_2 content of the injection fluid is closer to the solubility limit (#A.a.1b, Figure 3b). If the matrix permeability is increased to 1×10^{-18} m^2 (simulation #A.a.2), the Sg distribution after 10,000 years becomes slightly different (Figure 3c). In this case, the free gas phase spreads much more within the low permeability matrix where a maximum Sg value of 0.378 is obtained just above the reservoir.

The next simulations are run with lower (#A.a.3) and higher permeability values (#A.a.4 and #A.a.5) for the reservoir as well as for the fracture zone domain. For a permeability of 5×10^{-16} m^2 for both the reservoir and fracture zone, the CO_2 flux at the surface at steady state is decreasing to 1 g m^{-2} d^{-1}. In contrast, a flux of 198 g m^{-2} d^{-1}of CO_2 is reached with a permeability of 5×10^{-14} m^2. Simulations #A.a.6 to #A.a.9 consider different permeabilities for the reservoir (5×10^{-15} to 1×10^{-14} m^2) and fracture zone domains (1×10^{-14} to

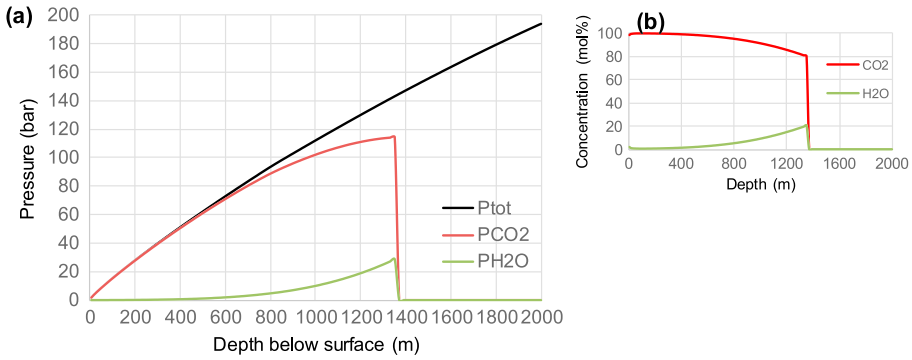

Figure 4. (a) CO_2-H_2O partial pressure in the CO_2-rich phase and total pressure profiles along the reservoir-fracture zone axis. (b) Corresponding CO_2 and H_2O concentrations in the CO_2-rich phase (mol %). Data are from simulation #A.a.1. at 10,000 years. The total pressure profile is slightly curved because of the temperature dependence of the water density.

1×10^{-13} m^2) to simulate a highly permeable fracture zone connected to a reservoir with a lower permeability. For this set of simulations, a maximum CO_2 flux of 238 g m^{-2} d^{-1} is reached when the permeability of the reservoir and the fracture zone is maximal (#A.a.9). This observation infers that CO_2 fluxes measured at the surface depend on the permeability of the reservoir as well as on the permeability of the fracture zone connecting the reservoir with the surface, i.e., CO_2 fluxes increase with the permeability of both domains. With a smaller surface area and volume for the fracture zone domain (#A.a.9b), the CO_2 surface is slightly increased to 265 g m^{-2} d^{-1}.

At steady state, the other surface parameters show little variations throughout the shallow exsolution simulations (#A). The temperature varies from 25.56 to 29.17°C and the gas saturation (Sg) from 0.15 to 0.17. For all simulations #A with geometry #a, the gas composition at the surface is almost pure CO_2 (approximately 98 mol %). The CO_2 flux at the surface is accompanied by a low liquid discharge (F_{liq} = 0.0004 to 0.058 kg s^{-1}) that is increasing with increasing permeability.

5.1.2. Geometry #b

The no-reservoir scenarios (geometry #b, Figure 2b) are run with a fracture zone permeability ranging from 5×10^{-15} to 1×10^{-13} m^2 (#A.b.1 to #A.b.4). CO_2 fluxes at the surface are reduced by about 20% compared to geometry type #a simulations under identical permeability conditions (#A.a.1, #A.a.4, and #A.a.5). Also, no significant differences in surface temperature, Sg, X_{CO2} and F_{liq} are observed when compared to geometry #a simulations. As an example, the Sg profile of simulation #A.b.1 is shown in Figure 3d. If the fracture zone permeability is increased from 5×10^{-15} m^2 to 1×10^{-13} m^2 (#A.b.4), CO_2 flux at the surface is increased from 12 to 405 g m^{-2} d^{-1} and the corresponding temperature increases from 25.64 to 33.45°C, which is well above the initial temperature of 25°C (Table 2).

For the 1×10^{-13} m^2 permeability no-reservoir scenario, the 10% overpressure at the injection area is reduced to 5% (#A.b.5). When compared to the corresponding 10% overpressure simulation (#A.b.4) the CO_2 flux at the surface is simply decreased by a factor of 2 and the surface temperature becomes 28.24°C (Table 2).

5.1.3. Geometry #c

For the large reservoir scenario (geometry #c) CO_2 fluxes and other physical parameters obtained at the surface (Sg, T, X_{CO2}, F_{liq}; Figure 3e) are similar to the ones obtained for the base-case scenario (geometry #a) under similar permeability conditions (#A.c.1, #A.c.2, #A.c.3 versus #A.a.1, #A.a.4, #A.a.5). Accordingly, we do not see an effect of the reservoir volume on CO_2 fluxes at the surface.

5.2. Deep Exsolution Simulations (#B)

The evolution of the gas saturation (Sg) for the deep exsolution simulations (#B) significantly differ from the ones obtained for the shallow exsolution simulations (#A). In particular, the gas phase migrates toward the caprock and the fracture zone domain much faster than for the shallow exsolution simulations. For instance, for the small reservoir scenario (geometry #a) with a reservoir and fracture zone permeability of 5×10^{-15} m^2

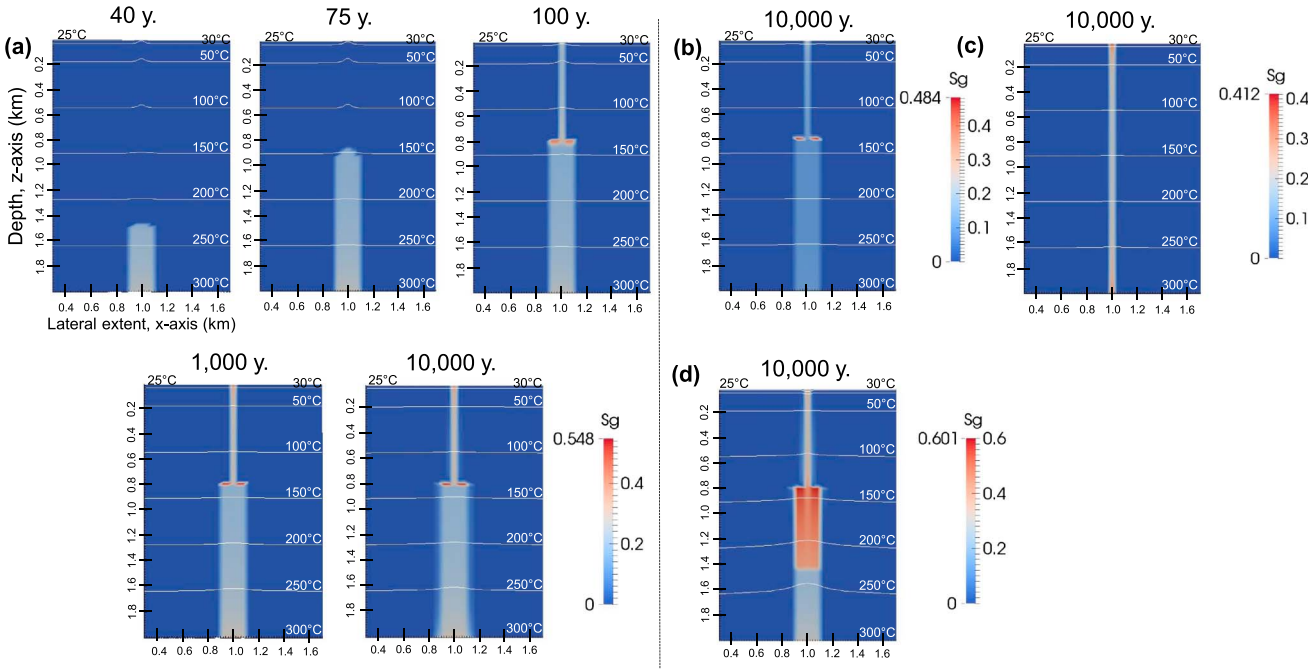

Figure 5. (a) Evolution of the gas saturation profile at different times of the simulation #B.a.1. (b–d) Sg profile at 10,000 years in simulations #B.a.5b, #B.b.1, and # B.c.1, respectively.

(simulation #B.a.1), it takes ~100 years for the CO_2-rich gas phase to fill the entire reservoir plus the fracture zone domain (Figure 5a). For this simulation CO_2 flux at the surface and the Sg distribution reach steady state conditions after approximately 130 years. The spatial Sg distribution (Figure 5a) is characterized by a maximum value of 0.55 within a narrow area below the caprock (40 m thick) and a value of 0.51 at the surface. These Sg values are thus much higher than the ones for simulations #A. By contrast, temperature and pressure profiles remain mostly similar to initial conditions and thus similar to the ones obtained for simulations #A (Figure 5a).

Throughout all simulations #B (#B.a.1 to #B.c.3) the surface CO_2 flux is between 345 and 37,461 g m^{-2} d^{-1}, and thus much larger than for the corresponding shallow exsolution simulations (#A) with the same permeability distribution (Table 2). Surface Sg values ranges from 0.26 to 0.51 and liquid fluxes vary from 0.00002 to 0.038 kg s^{-1}. If the gas saturation of the injection is lower (i.e., lower CO_2 content of the injected fluid), the CO_2 flux at the surface decreases significantly (#B.a.5: 16,115 g m^{-2} d^{-1} versus #B.a.5b: 433 g m^{-2} d^{-1}), although the maximum Sg value within the modeled domain only slightly decreases (Figure 5b).

Among the similarities shared with simulations #A, most simulations #B produce an almost pure CO_2 gas phase at the surface (X_{CO2} is ≥98 mol %) and surface temperatures that are close to initial conditions (25°C) even when the corresponding CO_2 fluxes are as high as 16,115 g m^{-2} d^{-1} (#B.a.5). However, for an extreme CO_2 flux of 37,461 g m^{-2} d^{-1} (#B.c.3: $k_{res} = 5 \times 10^{-14}$ m^2; $k_{fracture} = 5 \times 10^{-14}$ m^2), the temperature at the surface increased to 42°C. Another similarity with simulations #A is that the magnitude of the simulated CO_2 fluxes at the surface also depends on the permeability of the reservoir-fracture system.

In contrast, for the deep exsolution simulations #B the CO_2 fluxes at the surface strongly depend on the chosen reservoir geometry, which is not the case for the shallow exsolution simulations #A (Table 2). For example, for the large reservoir scenario (geometry #c), CO_2 fluxes are 3 times higher than for the small reservoir scenario (geometry #a) at the same permeability distribution (e.g., #B.c.1: 4892 g m^{-2} d^{-1} versus #B.a.1: 1634 g m^{-2} d^{-1}). Moreover, fluxes from the no-reservoir scenario (geometry #b) are 5 times lower than for the corresponding small reservoir scenario (e.g., #B.b.1: 345 g m^{-2} d^{-1} versus #B.a.1: 1634 g m^{-2} d^{-1}). The strong dependence of surface CO_2 fluxes on reservoir geometry is also reflected by the steady state Sg distributions

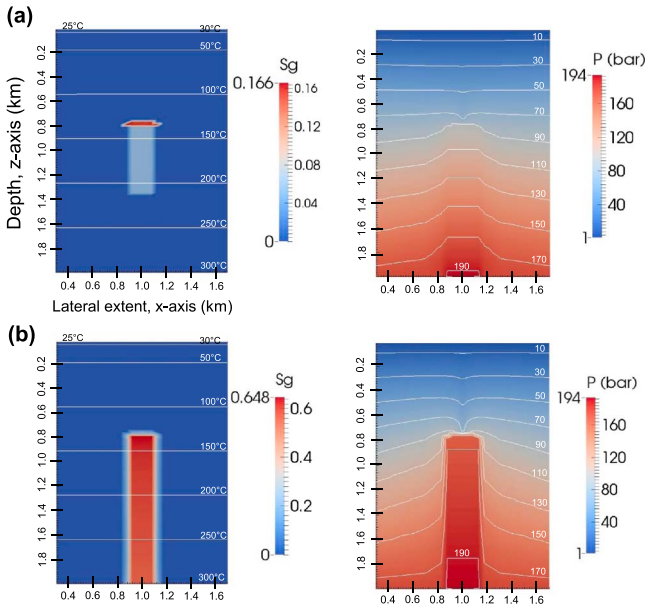

Figure 6. Sg and *P* profiles at the end of stage 2 in simulations (a) #A.a.10 and (b) #B.a.10. The pressure profile at the left and right side of the matrix domain corresponds to the initial hydrostatic pressure profile.

for the no-reservoir, small and large reservoir scenarios (Figures 5a, 5c, and 5d). For instance, in the large reservoir scenario (#B.c.1) the domain with elevated gas saturations (0.5 to 0.6) extends much deeper when compared to the corresponding small reservoir scenario (#B.a.1, Figure 5a).

To test the effect of an increased injection rate, simulations #B.a.2 and #B.a.3 are performed with an injection pressure increasing the hydrostatic pressure by 5 and 10%, respectively. In doing so, the CO_2 flux at the surface increased by 5% and 10%, respectively, while surface temperatures did not vary much (Table 2). It should be noted that the CO_2 flux increase is significantly different from the one obtained for the shallow exsolution simulation, for which the CO_2 flux is doubled when the overpressure is increased from 5 to 10%.

5.3. Transient Sealing Simulations

The transient sealing of the reservoir and its effects on the superficial CO_2 degassing are evaluated for both types of injections. Conditions inherited at the end of specific simulations #A and #B (subsequently referred to as stage 1) are used as initial conditions for these transient sealing simulations. In particular, for simulating transient sealing assuming shallow CO_2 exsolution as well as a small reservoir scenario (#A.a.10) the steady state conditions from simulation #A.a.7 ($k_{res} = 5 \times 10^{-15}$ m^2; $k_{fracture} = 1 \times 10^{-13}$ m^2) are chosen as initial conditions. In contrast, the steady state conditions from simulation #B.a.3 ($k_{res} = 5 \times 10^{-15}$ m^2; $k_{fracture} = 5 \times 10^{-15}$ m^2) are used to simulate transient sealing under deep exsolution conditions also assuming a small reservoir scenario (#B.a.10). Similar dynamics of degassing are obtained when using the permeability distribution from other single stage simulations (Table 2).

For both sealing simulations, the entire fracture zone domain is sealed by assigning a low permeability of 1×10^{-20} m^2. The simulations are then run for 10,000 years, which is subsequently referred to as stage 2. After that period, the fracture zone permeability is set to the same values as during stage 1 (1×10^{-13} m^2 for #A.a.10 and 5×10^{-15} m^2 for #B.a.10), and the simulation is rerun for another period of 10,000 years (subsequently referred to as stage 3).

Figure 6 shows the Sg, temperature, and pressure distributions at the end of the sealing period (i.e., stage 2) for both three stages sealing simulations. Under shallow exsolution conditions, the maximum Sg value within the gas pocket is 0.166. This value is restricted to a thickness of 40 m beneath the caprock. Instead, when injecting a CO_2-rich gas phase, the Sg value is greater than 0.5 for the whole reservoir domain ($Sg_{max} = 0.648$). The pressure distribution within the reservoir domain of the shallow exsolution simulation

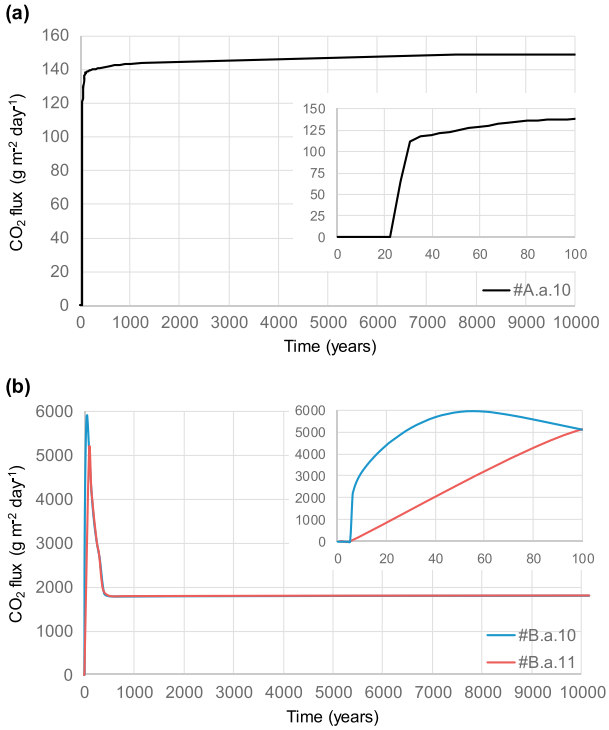

Figure 7. Evolution from 0 to 10,000 years (with an enlargement on the first 100 years) of surface CO_2 fluxes after the fracture zone is reopened (stage 3) in simulations (a) #A.a.10 and (b) #B.a.10 and #B.a.11.

(#A) indicates a profile similar to a hydrostatic pressure distribution (+10% overpressure), while for the deep exsolution simulation the profile within the reservoir is more similar to a vapor static pressure profile (low-pressure gradient). In this latter case, the pressure at the top of the reservoir domain (168 bar at 800 m depth) is much higher than the hydrostatic pressure (82 bar). This pressure, however, is still below the lithostatic pressure (204 bar), thus showing that this sealing simulation still refers to a stable condition.

Depending on the injection scenario, the gas reaches the surface after 23 (shallow exsolution simulation) or 6 years (deep exsolution simulation), respectively, once the fracture zone is reopened (Figure 7). In case of the shallow exsolution scenario (#A.a.10) the CO_2 flux at the surface is slowly approaching the one obtained for the corresponding single stage scenario at steady state (i.e., 147 g m^{-2} d^{-1} for #A.a.7, Table 2). In contrast, for the deep exsolution scenario (#B.a.9) the CO_2 flux reaches a transient maximum of ~6000 g m^{-2} d^{-1} after 60 years before approaching the steady state value obtained for the corresponding single stage scenario (i.e., 1800 g m^{-2} d^{-1} for #B.a.3; Table 2).

Additionally, two stages simulations (stages 2 and 3) are performed without stage 1 for both injection scenarios to simulate the degassing within a system initially sealed and filled with pure water (#A.a.11 and #B.a.11). In doing so, the fracture zone domain is initially sealed by assigning a permeability of 1×10^{-20} m^2. Fluid injection at the bottom of the reservoir occurs during 10,000 years. After this period, no free gas phase develops for the shallow exsolution scenario (#A.a.11), while a Sg distribution almost identical to the one of simulation #B.a.10 at the end of stage 2 (Figure 6b) is obtained for the deep exsolution simulation (#B.a.11). If the permeability of the fracture zone domain is reset to 5×10^{-15} m^2 for the deep exsolution simulation, the evolution of the CO_2 flux at the surface is similar to the one obtained during stage 3 of the deep exsolution, three stages sealing simulation (i.e., #B.a.10) but with a lower maximum, transient value (Figure 7b).

6. Discussion

6.1. Mutual Solubility of CO_2 and H_2O at High *P-T* Conditions

Only a few studies describe the formation of shallow CO_2-rich gas pockets in natural systems [i.e., *Giggenbach et al.*, 1991; *Sorey et al.*, 1998; *Chiodini et al.*, 1999, 2010]. For example, *Giggenbach et al.* [1991] describe the formation of a gas pocked starting from a condensed magmatic fluid that is water dominated and injected within the deep portion of a hypothetical hydrothermal system at a temperature of 400°C and at a hydrostatic pressure distribution (~800 bars) corresponding to a depth of ~ 8 km [*Giggenbach et al.*, 1991, Figure 5]. In this particular case, the temperature gradient is much lower than in our model as well as at our field site and the CO_2 content of the condensed magmatic fluid is considered to be $>$ 10 mol %. Moreover, *Giggenbach et al.* [1991] assume that the CO_2 content is partially reduced (buffered) because it interacts with primary silicates (Ca-Al silicates) to form secondary minerals such as clays and calcite. The remaining CO_2 content depends on the degree of water-rock interaction (e.g., surface area and residence time). Upon rising and leaving the buffering zone, the CO_2 solubility decreases in response to the decrease in temperature and pressure. A free CO_2 phase forms when the sum of P_{CO2} and P_{vap} overcomes the liquid pressure (i.e., hydrostatic pressure).

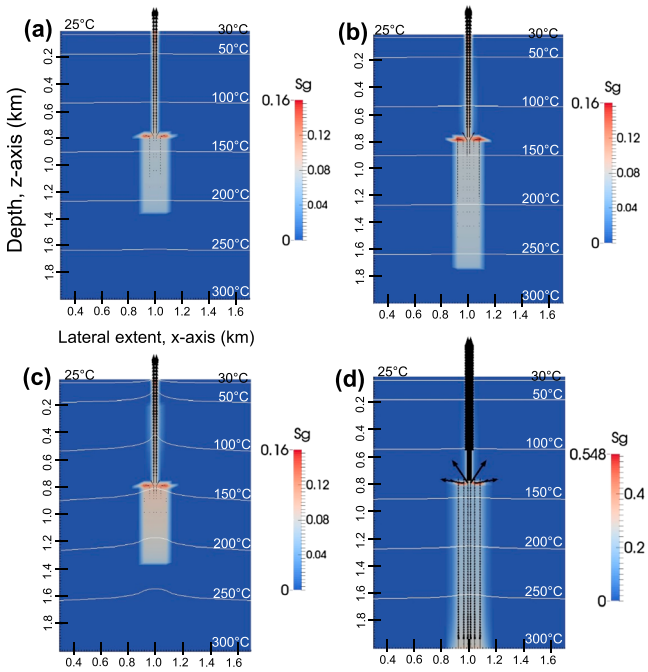

Figure 8. CO_2 flux vectors in simulations (a) #A.a.1, (b) #A.a.1b, (c) # A.a.9, and (d) #B.a.1 at 10,000 years. Sg and temperatures profiles are shown in the background. Note that compared to Figures 8a and 8b the vector intensities in Figures 8c and 8d are scaled down by a factor of 15 and 67, respectively. The size of the vectors at the surface corresponds to the CO_2 flux values reported in Table 2 for the illustrated simulations.

It should be noted that the *Giggenbach et al.* [1991] conceptual model considers the CO_2 solubility based on Henry's law as well as on the saturation pressure for pure water and does not take into account the mutual solubility of CO_2 and H_2O. Accordingly, some differences are observed between the *Giggenbach et al.* [1991] model and our simulations. For example, at a temperature of 300°C, the P_{vapor} is 86 bar while according to Henry's law the P_{CO2} at a CO_2 content of 5 mol % is 186 bar (Henry constant for CO_2 = 372 MPa), yielding a total gas pressure of 272 bar. This means that with these considerations at 300°C, a free gas phase forms when the water pressure becomes lower than 272 bar. Moreover, such a gas phase would be constituted of 68.4 mol % CO_2 and 31.6% H_2O. In contrast, assuming the mutual solubility of H_2O and CO_2 [*Spycher and Pruess*, 2010], a fluid with 5 mol % CO_2 would start to exsolve CO_2 at a total pressure of 300 bar, which is 28 bar higher than when following the *Giggenbach et al.* [1991] model. Using the *Spycher and Pruess* [2010] model the composition of the gas phase corresponds to 51.3 mol % of CO_2 and 48.6 mol % of H_2O, which is also different from the *Giggenbach et al.* [1991] model. Although the exsolution pressure and gas composition differences might seem insignificant, simulating the CO_2 exsolution dynamic over time using the *Giggenbach et al.* [1991] model would lead to a faster enrichment of CO_2 within the reservoir domain because it assumes a lower CO_2 solubility. Furthermore, in systems like Acoculco where the temperature gradient is high, the depth of gas exsolution is highly sensitive to the CO_2 dissolved content (simulation #A versus simulation #B). Therefore, ignoring the mutual solubility of H_2O and CO_2 under high *P-T* conditions can lead to distinct and thus erroneous modeling results.

6.2. Insights Into the Reservoir Geometry and Dissolved CO_2 Content

The surface CO_2 fluxes obtained at the end of the shallow exsolution (#A) simulations are much lower (1–405 g m^{-2} d^{-1}) than the highest CO_2 flux population measured at Alcaparrosa (mean: 5543 g m^{-2} d^{-1}) [*Peiffer et al.*, 2014]. Even when considering different reservoir geometries (Figure 2), the surface flux does not vary significantly (Table 2). Conversely, the surface fluxes obtained at the end of the deep exsolution simulations (#B) are much higher (345–37,461 g m^{-2} d^{-1}) and similar to the ones measured at Alcaparrosa.

The difference in the CO_2 flux magnitude between the scenarios #A and #B are illustrated in Figure 8, showing CO_2 flux vectors within the plane of injection for simulations #A.a.1, #A.a.1b, #A.a.9, and #B.a.1. For the shallow exsolution simulations (e.g., #A.a.1, #A.a.1b, and #A.a.9), most of the CO_2 exsolves from the water rising within

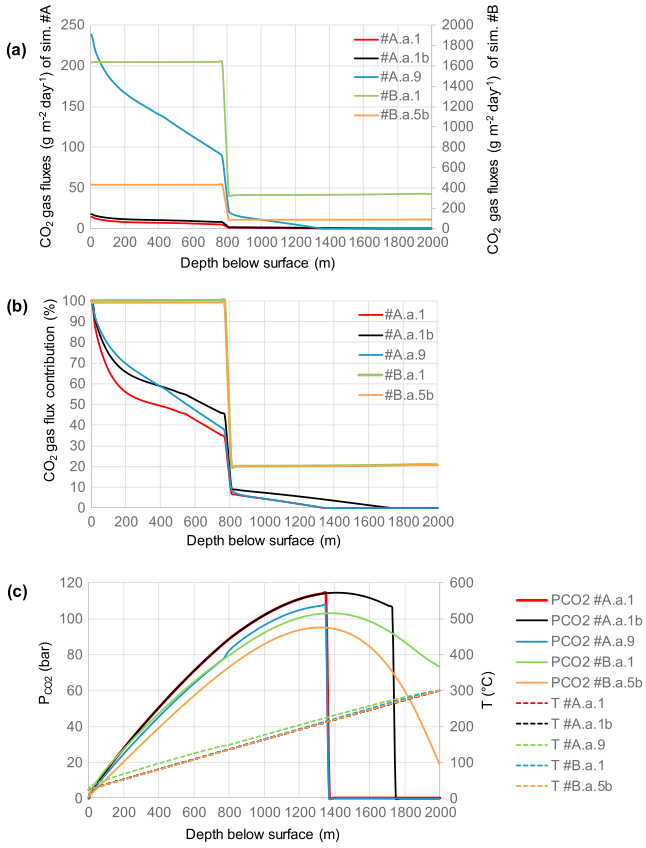

Figure 9. (a) Vertical (z) CO_2 fluxes (g m^{-2} d^{-1}) along the reservoir-fracture zone axis for simulations #A.a.1, #A.a.1b, #A.a.9, #B.a.1, and #B.a.5b at 10,000 years. (b) Corresponding gas flux contribution profiles. (c) Corresponding P_{CO2} and temperature profile. Note that Figure 9b is a normalization (%) of Figure 9a allowing a direct comparison between the different simulations.

the fracture zone and not from upflowing water within the reservoir (Figures 8a to 8c). Accordingly, the exsolved CO_2-rich gas phase cannot accumulate significantly in the reservoir (Figures 9a and 9b). For example, in simulation #A.a.1, 65% of the CO_2 exsolves within the fracture zone domain (Figure 9b). If the CO_2 content of the injection fluid is higher but still below the solubility limit (#A.a.1b), CO_2 first exsolves at a deeper depth (1750 m, Figures 8b and 9c), but surprisingly, most of the CO_2 (55%) still exsolves within the fracture (Figure 9b). Similarly, simulation #A.a.9 which simulates a higher permeability reservoir and fault zone (#A.a.9, Figure 9b) is also characterized by a major CO_2 exsolution within the fracture (62%), even though the CO_2 flux is larger than for most other simulations #A (Table 2). All these observations are the consequence of the high-temperature gradient at Acoculco (Figure 9c) that does not yield major CO_2 exsolution at a deeper depth because the CO_2 solubility is too high at such conditions, even when the CO_2 content of the injection fluid is close to the solubility limit. Minor CO_2 exsolution occurring within the reservoir domain is therefore the reason why for the shallow exsolution simulations (#A) the CO_2 flux at the surface is not sensitive to the size of the reservoir (Table 2). Furthermore, the gas saturation in all simulations #A remains low within the whole domain which induces a higher relative permeability for the liquid phase. Therefore, CO_2 is more efficiently transported in a dissolved state rather than as a CO_2-rich gas phase. Actually, in simulations #A surface CO_2 fluxes are linearly correlated ($r^2 = 0.999$) with liquid discharge at the surface (Table 2).

In the deep exsolution simulations, the horizontal slope characterizing the CO_2 flux profiles within the fracture zone and the reservoir domains (#B.a.1 and #B.a.5b, Figures 9a and 9b) demonstrates that most of the CO_2 transported in the gas phase toward the surface corresponds to the CO_2-rich gas phase injected at the bottom of the domain. The sharp change in slope of the cumulated flux observed at a depth of 800 m for simulations #B reflects the important gas accumulation at the top of the reservoir domain (Figure 9b). This change in slope is much less pronounced for simulations #A, indicating that gas accumulation within the reservoir is less significant. The different CO_2 exsolution depth is the main reason why the CO_2 flux at the surface is only sensitive to the reservoir geometry in case of the deep exsolution scenarios (Table 2). This is a major conclusion from our large set of simulations: if CO_2 exsolution mainly occurs at a shallower depth than the top of a geothermal reservoir (i.e., within an overlying fracture network such as in our simulations #A), then CO_2 flux at the surface will only depend on the rock permeability, the dissolved CO_2 content of the deep fluid, and the P-T gradient, but not on the size of the reservoir.

Overall, the deep exsolution simulations (#B) produce surface CO_2 fluxes similar to the ones measured at Alcaparrosa. Accordingly, a scenario similar to one of our simulations #B is considered to be the most realistic scenario to explain the features observed at Acoculco (e.g., CO_2 flux measurements). Another justification

reinforces this hypothesis. In simulations #B, the gas phase reaches the surface at a similar flux than the one injected at the bottom domain (Figure 9a). Therefore, the application of gas geothermometers (e.g., CO_2/CH_4 and CO_2/Ar) to the gas sampled at the surface should predict a temperature close to the one of equilibration within the liquid phase (i.e., the temperature of the reservoir) assuming that no reequilibration occurs on the way to the surface. On the opposite, in simulations #A, if the dissolved CO_2 of the injected fluid is such that CO_2 mainly exsolves within the shallow fracture zone where the temperature is lower, the CO_2/Ar and CO_2/CH_4 gas geothermometers applied to a gas sampled at the surface would indicate temperatures significantly lower than 300°C, as demonstrated by using different temperatures of separation in Table 1. In simulation #A.a.1, 50% of the total gas phase is exsolved in the upper ~300 m of the fracture zone (Figure 9b). Considering this depth and a corresponding temperature of 65°C (Figure 9c), the CH_4/CO_2 ratio in the gas phase (in equilibrium with the liquid phase) formed at this temperature would lead to a geothermometer estimate of 224°C, while the CO_2/Ar would indicate a temperature of 242°C (Table 1). If the dissolved gases reequilibrate with the wall rock between the deeper part of the reservoir and the fracture, the temperature estimates would be even lower. Because ECO2N does not allow to consider CH_4 nor Ar components in the simulations, these calculation are performed using Henry's law coefficients for each gas in conjunction with equations (3) and (4). Since the gas geothermometers' results for Acoculco gases point to higher temperatures (306°C ± 58°C), simulations #A appear to be an unrealistic scenario for Acoculco.

In contrast to estimating the CO_2 exsolution depth, it is more challenging to assess the actual reservoir geometry for the Acoculco geothermal system. The main challenge is that based on our deep exsolution simulations (#B), any kind of reservoir geometry can reproduce the high CO_2 fluxes measured at Acoculco (mean: 5543 g m^{-2} d^{-1}, Table 2) if the permeability distribution and the CO_2 content are specified accordingly. In particular, in order to produce high CO_2 fluxes at the surface assuming a small or no reservoir scenario, the gas saturation of the injection fluid has to be high to get elevated CO_2 fluxes such as observed at Acoculco: e.g., simulation #B.a.5 shows much higher CO_2 fluxes at the surface compared to simulation #B.a.5b because of the higher gas saturation of the injection fluid (Table 2). CO_2 exsolution from the deep fluid must thus occur below a depth of 2000 m, and the formed CO_2-rich gas phase has to accumulate somewhere to induce an elevated gas saturation and subsequent high CO_2 flux at the surface. This line of arguments leads to the hypothesis of a reservoir at depth greater than 2000 m. The size of this reservoir, however, cannot be estimated using a modeling approach such as presented here because of the temperature limitation of ECO2N.

6.3. Geothermobarometry Considerations

Although the solubility data of CO_2 in water above 300°C are not yet available, the depth of the hypothetical reservoir can be roughly estimated. The observation that by specifying a dissolved CO_2 concentration of 5 mol % for the injected CO_2-rich phase allowed simulating high fluxes similar to the ones measured in the field [*Peiffer et al*., 2014] suggests that such a CO_2 content represents a reasonable assumption. To estimate the actual reservoir depth, we first consider CO_2 solubility at 300°C because it is not known for higher temperatures. According to *Spycher and Pruess* [2010], a maximum CO_2 solubility of 5 mol % at 300°C is obtained at a pressure of 300 bar, which corresponds to a depth of ~3000 m assuming hydrostatic pressure distribution. Since the solubility of CO_2 increases with temperature (above ~155°C) and because our simulations suggest that the reservoir temperature is above > 300°C, we suspect that CO_2 is fully dissolved at 300 bar. From our simulations we know that we can only get high CO_2 fluxes at the surface as observed at Acoculco if CO_2 exsolves below the top of a reservoir. Accordingly, we propose that at Acoculco, a geothermal reservoir with unspecified size is located at pressure lower than 300 bar and presumably between 2000 and 3000 m depth.

Another approach can be used to narrow down this depth interval. *Giggenbach* [1991] derived a CO_2 geobarometer/geothermometer based on the assumption that the dissolved CO_2 content of a fluid is buffered by the same minerals as the ones considered in the CO_2/Ar geothermometer:

$$\text{Log } P_{CO2} = 0.0168\,T - 3.78 \quad (6)$$

with T in °C and P_{CO2} in bar.

Assuming that the partial CO_2 pressure of the injection fluid in simulations #B (73 bar) is at equilibrium with wall rock minerals, a corresponding temperature of 336°C is obtained, which is within the temperature range obtained applying gas geothermometers (equations (1) and (2)) to Acoculco gas samples (Table 1). This

consideration suggests that the hypothetical geothermal reservoir at Acoculco should hence be located close to our model limit. Considering a temperature gradient of 140°C/km, the corresponding depth would be some 2260 m below surface.

6.4. Transient Sealing and Buoyancy-Driven CO_2

By analogy to the "opened fracture" simulations (one stage, #A.a.1 to B.c.3), the transient sealing simulations (two and three stages simulations, Table 2) demonstrate that there is no significant gas accumulation within the reservoir domain for the shallow exsolution simulations (#A) (Figure 7a). On the opposite, the peak characterizing the CO_2 flux evolution of simulation #B.a.10 reflects important gas accumulation within the reservoir when injecting a CO_2-rich gas phase (Figure 7b). Interestingly, when the fracture zone is reopened (stage 3), CO_2 reached the surface much sooner in case of the deep exsolution scenarios (#B.a.10: 6 years; #A.a.10: 23 years), even under low permeability conditions (Figures 7a and 7b, inserts). This observation is caused by the higher pressure at the top of the reservoir domain at the end of the sealing period, as well as by the higher gas saturation of the accumulated gas phase (stage 2, Figures 6a and 6b). Time delays between seismic events and surface degassing peaks (e.g., in simulation #B.a.10 the delay between fracture zone reopening and the CO_2 degassing peak at the surface) are well-known phenomena in volcanic and geothermal areas. It is assumed that such delays reflect a pressurization event caused by CO_2-rich fluid accumulation within the reservoir and the subsequent fluid transport to the surface. At Mammoth Mountain, characteristic delays of 2–3 years were observed between seismic events and corresponding surface degassing peaks [*Werner et al.*, 2014].

When injecting a single-phase liquid with dissolved CO_2 within a sealed reservoir initially filled with pure water (two stages simulation #A.a.11), CO_2 remains in dissolved state during the entire sealing period (not shown). The continuous injection of liquid within the sealed reservoir induces a pressure build up within the reservoir, impeding thus the dissolved CO_2 and water vapor to exsolve. The pressure increase is accompanied by a pressure gradient decrease within the reservoir. Accordingly, the injection rate is continuously decreasing. By contrast, for the corresponding deep exsolution simulation #B.a.11, a gas pocket is able to form even if the pressure builds up over time, because gas migration is mainly occurring due to buoyancy forces. Sg and *P* distributions at the end of stage 2 in this simulation are similar to the ones obtained in simulation #B.a.10 (Figure 6b).

CO_2 upflow occurring due to buoyancy forces is assumed to cause the low sensitivity of the CO_2 flux at the surface on the specified overpressure observed for the deep exsolution scenarios. For instance, doubling the overpressure from 5 to 10% only increased the surface CO_2 flux from 1717 to 1793 $g\,m^{-2}\,d^{-1}$ (#B.a.2 versus #B.a.3, Table 2). Simulations #B thus demonstrate that only a small fraction of the total surface flux originate from the exsolution of dissolved CO_2 within the model domain, while the remaining fraction corresponds to CO_2 driven by buoyancy from depth. In contrast, for the simulations #A, the liquid and CO_2 fluxes reaching the surface are directly scaled to the increase in overpressure (#A.b.4 versus #A.b.5, Table 2), because below the depth where major exsolution occurs, most CO_2 is dissolved and transported by liquid advection.

6.5. Surface Temperatures

The surface temperatures in the shallow exsolution simulations (#A) range from 25.56°C to 33.45°C. They are linearly correlated ($r^2 = 0.907$) to the flux of liquid water reaching the surface through the fracture zone (Table 2), indicating that the heat is mainly carried by liquid water.

The water flux depends on the fracture zone permeability but also on the relative permeability of the liquid phase. The higher the gas saturation, the more reduced the relative permeability of the liquid phase. For this reason, most deep exsolution simulations (#B), except #B.c.3 ($T = 42.45$°C), show no significant temperature increase at the surface at steady state. In contrast, for some of the simulations #B, temperatures slightly below ($T_{min} = 23.85$°C) the initial temperature are obtained depending on the reservoir geometry and permeability distribution (Table 2). The temperatures lower than 25°C reflect a temperature drop caused by CO_2 volume expansion when CO_2 rises up toward the surface and the pressure decreases. If the CO_2 upflow is fast enough, the heat exchange with the surrounding rocks is limited causing the temperature to decrease. Under an ideal situation with no heat exchange, the volume expansion is isenthalpic causing the temperature of the gas phase to decrease significantly. This mechanism is known to cause impressive temperature drop: solid CO_2 particles (dry ice) are observed in some oil wells where CO_2 is used for enhancing recovery [*Pruess*, 2008]. Nevertheless, in the concerned simulations (#B.a.5, #B.c.1, and #B.c.2), the drop in temperature is very limited

(maximum 1.25°C in #B.c.2) because heat exchange by conduction with the wall rock is dominant here. Furthermore, the high-temperature gradient used in the simulations impedes to have any significant temperature drop below the surface temperature. Considering that the injected CO_2 is submitted to isenthalpic expansion from the depth of 2000 m ($P = 176.3$ bar, $T = 300$°C, CO_2 enthalpy = 732 kJ/kg) to the surface, the corresponding CO_2 temperature under atmospheric pressure would be 263°C, a drop of 37°C due to expansion. If ignoring the thermal energy converted into gravitational potential energy and kinetic energy (not computed by TOUGH2), the heat loss through conduction with the surrounding formations will then be responsible for the remaining ~238°C drop, allowing a surface temperature within the fracture zone close to 25°C. In geothermal systems with lower temperature gradient, the temperature drop due to expansion would be more important. For a deep CO_2 fluid temperature at 125°C and a similar pressure of 176.3 bar (CO_2 enthalpy 492 kJ/kg), the temperature of CO_2 at the surface would be 9°C without considering heat exchange with the surrounding wall rock.

Simulation #B.c.3 shows a higher surface temperature (42.45°C). In this case the heat flux carried by CO_2 over the simulation period exceeds the heat lost by conduction and the thermal effect caused by some limited volume expansion, so the temperature is able to increase. This simulation is nevertheless unrealistic since no thermal anomalies were observed in the studied area. The take home message is that there is a critical value of surface CO_2 flux (e.g., ~37,000 g m^{-2} d^{-1}, #B.c.3) at which the heat flux carried by CO_2 cannot be balanced anymore, causing the surface temperature to increase even though the CO_2 enthalpy is much lower than the one of water vapor.

7. Conclusions

We performed numerical modeling of CO_2 flux soil measurements to get some insights into the dynamic of cold magmatic CO_2 degassing, and more specifically into a hidden geothermal system characterized by a high temperature gradient, the Acoculco caldera (Mexico). Through a large set of heat and multiphase fluid flow simulations, we quantitatively explored the relationship between field-scale CO_2 soil flux measurements and several parameters such as the reservoir geometry, the rock permeability, and the CO_2-dissolved content of the deep reservoir fluid. The ECO2N V2.0 equation of state was used to compute the mutual solubility of CO_2 and H_2O, which is important to account for at high *P-T* conditions. In fact, it was shown that a variation of a few decimals of mol % in the dissolved CO_2 concentration can lead to significantly different dynamics of degassing (shallow versus deep exsolution). It is thus concluded that under high-temperature gradient conditions the depth of major CO_2 exsolution is highly sensitive to the dissolved CO_2 content. Modifying the permeability of the rocks does not significantly modify the exsolution profile but does affect the fluid fluxes (gas and liquid) that reach the surface. If the gas exsolution occurs mainly below the top of the reservoir, then surface gas fluxes will be sensitive to the gas saturation state of the deep fluid as well as the size of the reservoir where the free gas phase accumulates. If exsolution occurs above the reservoir, the surface degassing will mainly depend on the permeability of the reservoir/fracture zone domains and the CO_2 dissolved content of the fluid at depth.

The fact that no thermal anomalies are observed at the surface in systems characterized by high CO_2 degassing is a consequence of the low enthalpy of CO_2 compared to vapor enthalpy. CO_2 may efficiently cool down by heat conduction with the wall rock and to a certain extent by isoenthalpic volume expansion depending on the temperature gradient conditions. This latter effect is more pronounced in systems with low-temperature gradients. Nevertheless, if the uprising CO_2 flux exceeds a critical threshold, in our simulations ~37,000 g m^{-2} d^{-1}, the heat flux becomes significant and cannot be balanced anymore, and hence, the surface temperature starts increasing.

Through this modeling effort, we have shown that some insights can be gained from limited CO_2 soil flux measurements to explore and characterize the conditions at depth in geothermal systems. Among the specific results obtained for the Acoculco site, we depict the following. By integrating the simulations results with gas geothermometry estimates, it was possible to affirm that the deep fluid at 2000 m depth has already boiled. In order to induce high CO_2 fluxes at the surface, this fluid must have a certain degree of gas saturation and requires the presence of a deeper reservoir where gas accumulation occurs. However, because the equation of state ECO2N V2.0 used in the simulations is limited to a maximum temperature of 300°C, the

exact depth at which CO_2 exolusion takes place could not be determined by this modeling analysis. Nevertheless, simulations' results and geothermobarometry considerations suggest that such a reservoir is located close to the lower boundary of the current model (2000 m depth). Since the rock permeability at Acoculco is known to be low as revealed by the well cuttings, the extent of this reservoir is probably small and restricted to some kind of fracture networks. In contrast, our simulations infer that the presence of a reservoir is not needed in the shallower 2000 m. Here the presence of a fracture zone is enough to reproduce high CO_2 flux at the surface provided that the deep fluid coming from the underlying reservoir has reached a high gas saturation. We believe that our numerical model would benefit from complementary studies, such as more extensive CO_2 flux measurements, geophysical surveys (vertical electric and magnetotelluric soundings), and exploratory drilling to at least 3000 m depth, to validate the presence of a deep reservoir.

Acknowledgments

All the data are available upon request to the authors. Lo.P. was supported by the CEMIE-GEO Conacyt-SENER project 09, the DGAPA-UNAM grant IT101014 and an internal IER-UNAM project. C.W. was supported by the Swiss Competence Center for Energy Research-Supply of Electricity (SCCER-SOE). Le.P. was funded by the Assistant Secretary for Energy Efficiency and Renewable Energy, Geothermal Technologies Program of the U.S. Department of Energy under contract DE-AC02-05CH11231. Authors would like to thank Antonio P. Rinaldi and Lauriane Chardot for their thorough review and constructive comments.

References

Bergfeld, D., F. Goff, and C. J. Janik (2001), Elevated carbon dioxide flux at the Dixie Valley geothermal field, Nevada; relations between surface phenomena and the geothermal reservoir, *Chem. Geol.*, *177*, 43–66.

Canet, C., B. Hernández-Cruz, A. Jiménez-Franco, T. Pi, B. Peláez, R. E. Villanueva-Estrada, P. Alfonso, E. González-Partida, and S. Salinas (2015), Combining ammonium mapping and short-wave infrared (SWIR) reflectance spectroscopy to constrain a model of hydrothermal alteration for the Acoculco geothermal zone, Eastern Mexico, *Geothermics*, *53*, 154–165.

Chiodini, G., W. D'Alessandro, and F. Parello (1996), Geochemistry of gases and waters discharged by the mud volcanoes at Paternò, Mt. Etna (Italy), *Bull. Volcanol.*, *58*, 51–58.

Chiodini, G., R. Cioni, M. Guidi, B. Raco, and L. Marini (1998), Soil CO_2 flux measurements in volcanic and geothermal areas, *Appl. Geochem.*, *13*, 543–552.

Chiodini, G., F. Frondini, D. M. Kerrick, J. Rogie, F. Parello, L. Peruzzi, and A. R. Zanzari (1999), Quantification of deep CO_2 fluxes from central Italy. Examples of carbon balance for regional aquifers and of soil diffuse degassing, *Chem. Geol.*, *159*, 205–222.

Chiodini, G., M. Todesco, S. Caliro, C. Del Gaudio, G. Macedonio, and M. Russo (2003), Magma degassing as a trigger of bradyseismic events: The case of Phlegrean Fields (Italy), *Geophys. Res. Lett.*, *30*(8), 1434, doi:10.1029/2002GL016790.

Chiodini, G., D. Granieri, R. Avino, S. Caliro, and A. Costa (2005), Carbon dioxide diffuse degassing and estimation of heat release from volcanic and hydrothermal systems, *J. Geophys. Res.*, *110*, B08204, doi:10.1029/2004JB003541.

Chiodini, G., D. Granieri, R. Avino, S. Caliro, A. Costa, C. Minopoli, and G. Vilardo (2010), Non-volcanic CO_2 Earth degassing: Case of Mefited'Ansanto (southern Apennines), Italy, *Geophys. Res. Lett.*, *37*, L11303, doi:10.1029/2010GL042858.

Fournier, N., and L. Chardot (2012), Understanding volcano hydrothermal unrest from geodetic observations: Insights from numerical modeling and application to White Island volcano, New Zealand, *J. Geophys. Res.*, *117*, B11208, doi:10.1029/2012JB009469.

Gerlach, T. M., M. P. Doukas, K. A. McGee, and R. Kessler (2001), Soil efflux and total emission rates of magmatic CO_2 at the Horseshoe Lake tree kill, Mammoth Mountain, California, 1995–1999, *Chem. Geol.*, *177*(1–2), 101–116.

Giggenbach, W. F. (1980), Geothermal gas equilibria, *Geochim. Cosmochim. Acta*, *44*, 2021–2032.

Giggenbach, W. F. (1991), Chemical techniques in geothermal exploration, in *Applications of Geochemistry in Geothermal Reservoir Development*, *Ser. Tech. Guides Use Geotherm. Energy*, edited by F. D'Amore, pp. 119–144, UNITAR/UNDP Center on Small Energy Resources, Rome.

Giggenbach, W. F. (1997), The origin and evolution of fluids in magmatic-hydrothermal systems, in *Geochemistry of Hydrothermal Ore Deposits*, 3rd ed., edited by H. L. Barnes, pp. 737–796, John Wiley, New York.

Giggenbach, W. F., Y. Sano, and H. U. Schminckle (1991), CO_2-rich gases from Lakes Nyos and Monoun, Cameroon; Laacher See, Germany; Dieng, Indonesia and Mt. Gambier, Australia, *J. Volcanol. Geotherm. Res.*, *45*, 311–323.

Hutnak, M., S. Hurwitz, S. E. Ingebritsen, and P. A. Hsieh (2009), Numerical models of caldera deformation: Effects of multiphase and multicomponent hydrothermal fluid flow, *J. Geophys. Res.*, *114*, B04411, doi:10.1029/2008JB006151.

Kiryukhin, A. V., and V. A. Yampolsky (2004), Modeling study of the Pauzhetsky geothermal field, *Geothermics*, *33*, 421–442.

Lewicki, J., and C. M. Oldenburg (2005), Near-surface CO_2 monitoring and analysis to detect hidden geothermal systems, in *Proceedings, Thirtieth Workshop on Geothermal Reservoir Engineering*, 8 pp., Stanford Univ., Stanford, Calif.

López-Hernandez, A., G. García-Estrada, G. Aguirre-Díaz, E. González-Partida, H. Palma-Guzmán, and J. Quijano-León (2009), Hydrothermal activity in the Tulancingo-Acoculco Caldera Complex, central Mexico: Exploratory studies, *Geothermics*, *38*, 279–293.

Lorenzo Pulido, C., M. Flores Armenta, and G. Ramírez Silva (2011), Caracterización de un yacimiento de roca seca caliente en la zona geotérmica de Acoculco, Pue, *Geotermia*, *24*(1), 59–69.

Manning, C. E., and S. E. Ingebritsen (1999), Permeability of the continental crust: Implications of geothermal data and metamorphic systems, *Rev. Geophys.*, *37*, 127–150, doi:10.1029/1998RG900002.

Mazot, A., D. Rouwet, Y. Taran, S. Inguaggiato, and N. Varley (2011), CO_2 and He degassing at El Chichón volcano, Chiapas, Mexico: Gas flux, origin and relationship with local and regional tectonics, *Bull. Volcanol.*, 73, 423–442.

McKenna, J. R., and D. D. Blackwell (2004), Numerical modeling of transient Basin and Range extensional geothermal systems, *Geothermics*, *33*, 457–476.

Mualem, Y. (1976), A new model for predicting the hydraulic conductivity of unsaturated porous media, *Water Resour. Res.*, *12*(3), 513–522, doi:10.1029/WR012i003p00513.

Pan, L., N. Spycher, C. Doughty, and K. Pruess (2014), *ECO2N V2.0: A TOUGH2 Fluid Property Module for Mixtures of Water, NaCl, and CO_2*, Lawrence Berkeley Natl. Lab., Berkeley, Calif.

Peiffer, L., R. Bernard-Romero, A. Mazot, Y. Taran, M. Guevara, and E. Santoyo (2014), Fluid geochemistry and soil gas fluxes (CO_2-CH_4-H_2S) at a promissory Hot Dry Rock Geothermal System: The Acoculco caldera, Mexico, *J. Volcanol. Geotherm. Res.*, *284*, 122–137.

Plyasunov, A. V., and E. L. Shock (2003), Prediction of the vapor–liquid distribution coefficients for volatile nonelectrolytes in water up to its critical temperature, *Geochim. Cosmochim. Acta*, *67*, 4981–5009.

Pruess, K. (2008), On CO_2 fluid flow and heat transfer behavior in the subsurface, following leakage from a geologic storage reservoir, *Environ. Geol.*, *54*(8), 1677–1686, doi:10.1007/s00254-007-0945-x.

Pruess, K., C. Oldenburg, and G. Moridis (1999), TOUGH2: User's guide, version 2.0 Rep. LBNL-43134, Lawrence Berkeley Natl. Lab., Berkeley, Calif.

Rinaldi, A., M. Todesco, and M. Bonafede (2010), Hydrothermal instability and ground displacement at the Campi Flegrei caldera, *Phys. Earth Planet. Inter.*, *178*, 155–161, doi:10.1016/j.pepi.2009.09.005.

Rinaldi, A., M. Todesco, J. Vandemeulebrouck, A. Revil, and M. Bonafede (2011), Electrical conductivity, ground displacement, gravity changes, and gas flow at Solfatara crater (Campi Flegrei caldera, Italy): Results from numerical modeling, *J. Volcanol. Geotherm. Res.*, *207*, 93–105, doi:10.1016/j.jvolgeores.2011.07.008.

Rinaldi, A. P., J. Vandemeulebrouck, M. Todesco, and F. Viveiros (2012), Effects of atmospheric conditions on surface diffuse degassing, *J. Geophys. Res.*, *117*, B11201, doi:10.1029/2012JB009490.

Serpen, U., and A. Niyazi (2005), Reinjection problems in overpressured geothermal reservoirs, in *Proceedings, Thirtieth Workshop on Geothermal Reservoir Engineering*, 8 pp., Stanford Univ., Stanford, Calif.

Sorey, M. L., W. C. Evans, B. M. Kennedy, C. D. Farrar, L. J. Hainswort, and B. Hausback (1998), Carbon dioxide and helium emissions from a reservoir of magmatic gas beneath Mammoth Mountain, California, *J. Geophys. Res.*, *103*, 15,303–15,323, doi:10.1029/98JB01389.

Spycher, N., and K. Pruess (2005), Mixtures in the geological sequestration of CO_2: II. Partitioning in chloride brines at 12–100°C and up to 600 bar, *Geochim. Cosmochim. Acta*, *69*, 3309–3320.

Spycher, N., and K. Pruess (2010), A phase-partitioning model for CO_2–brine mixtures at elevated temperatures and pressures: Application to CO_2-enhanced geothermal systems, *Transp. Porous Med.*, *82*(1), 173–196.

Spycher, N., K. Pruess, and J. Ennis-King (2003), CO_2-H_2O mixtures in the geological sequestration of CO_2: I. Assessment and calculation of mutual solubilities from 12 to 100°C and up to 600 bar, *Geochim. Cosmochim. Acta*, *67*, 3015–3031.

Todesco, M., A. P. Rinaldi, and M. Bonafede (2010), Modeling of unrest signals in heterogeneous hydrothermal systems, *J. Geophys. Res.*, *115*, B09213, doi:10.1029/2010JB007474.

van Genuchten, M. T. (1980), A closed-form equation for predicting the hydraulic conductivity of unsaturated soils, *Soil Sci. Soc.*, *44*, 892–898.

Viggiano Guerra, J. C., M. Flores Armenta, and G. Ramírez Silva (2011), Evolución del sistema geotérmico de Acoculco, Pue., México: Un estudio con base en estudios petrográficos del pozo EAC-2 y en otras consideraciones, *Geotermia*, *24*(1), 14–24.

Viveiros, F., C. Cardellini, T. Ferreira, S. Caliro, G. Chiodini, and C. Silva (2010), Soil CO_2 emissions at Furnas volcano, São Miguel island, Azores archipelago: Volcano monitoring perspectives, geomorphologic studies, and land use planning application, *J. Geophys. Res.*, *115*, B12208, doi:10.1029/2010JB007555.

Viveiros, F., J. Vandemeulebrouck, A. P. Rinaldi, T. Ferreira, C. Silva, and J. V. Cruz (2014), Periodic behavior of soil CO_2 emissions in diffuse degassing areas of the Azores archipelago: Application to seismovolcanic monitoring, *J. Geophys. Res. Solid Earth*, *119*, 7578–7597, doi:10.1002/2014JB011118.

Wanner, C., L. Peiffer, N. Spycher, E. Sonnenthal, B. M. Kennedy, and J. Iovenitti (2014), Reactive transport modeling of the Dixie Valley geothermal area: Insights on flow and geothermometry, *Geothermics*, *51*, 130–141.

Werner, C., D. Bergfeld, M. P. Doukas, C. D. Farrar, P. J. Kelly, and C. Kern (2014), Decadal-scale variability of diffuse CO_2 emissions and seismicity revealed from long-term monitoring (1995–2013) at Mammoth Mountain, California, USA, *J. Volcanol. Geotherm. Res.*, *289*, 51–63.